



Morphotype differentiation in the Great Barrier Reef *Halimeda* bioherm carbonate factory: Internal architecture and surface geomorphometrics

Mardi A. McNeil¹ | Luke D. Nothdurft¹ | Nicholas J. Dyriw¹ | Jody M. Webster² | Robin J. Beaman³

¹School of Earth and Atmospheric Sciences, Queensland University of Technology, Brisbane, Qld, Australia

²Geocoastal Research Group, School of Geosciences, The University of Sydney, Sydney, NSW, Australia

³College of Science and Engineering, James Cook University, Cairns, Qld, Australia

Correspondence

Mardi A. McNeil, School of Earth and Atmospheric Sciences, Science and Engineering Faculty, Queensland University of Technology, Brisbane, Qld, Australia.
Email: ma.mcneil@qut.edu.au

Funding information

The Ian Potter Foundation National Geographic Society, Grant/Award Number: EC-190R-18; The Great Barrier Reef Marine Park Authority, Grant/Award Number: Reef Guardians science grants; The National Parks and Wildlife Foundation

Abstract

The calcareous *Halimeda* bioherms of the northern Great Barrier Reef, Australia are the largest actively accumulating *Halimeda* deposits worldwide. They contribute a substantial component of the Great Barrier Reef neritic carbonate factory, as well as the geomorphological development of Australia's northeast continental shelf. *Halimeda* bioherm geomorphology is complex, expressing three distinct variations in morphotype patterns: annulate, reticulate and undulate. Similar regular and irregular geomorphological patterning often results from scale-dependent biophysical feedback mechanisms. Therefore, a better understanding of morphotype differentiation can inform the biotic and abiotic drivers of spatial heterogeneity in the bioherm ecosystem. Here, 3D LiDAR bathymetry is integrated with 2D sub-bottom profile datasets to investigate surface topography and internal sedimentary architecture of *Halimeda* bioherms through space and time. Using the ESRI ArcGIS 3D Analyst and Benthic Terrain Modeller extensions, the bioherm surface and subsurface geomorphometric characteristics were quantified for the annulate, reticulate and undulate morphotypes. Significant variation was found between the three bioherm morphotypes in their surface topography, internal structure, volume, slope gradients and terrain complexity. Therefore, their geomorphology is probably influenced by differing processes and biophysical feedback mechanisms. The complex surface topography does not appear to be inherited from the antecedent substrate, and preferred aspect orientations resulting from hydrodynamic forcing appear to be limited. It is suggested here that autogenic dynamics or biotic self-organization similar to patterns and processes in other marine organo-sedimentary systems modulates *Halimeda* bioherm geomorphology, and some hypotheses are offered towards future studies. Morphotype differentiation has implications for the development of the *Halimeda* bioherm carbonate factory, rates of sediment aggradation and progradation, and variable capacity to fill accommodation space. Self-organization dynamics and morphology differentiation in Modern bioherm systems could potentially inform

This is an open access article under the terms of the Creative Commons Attribution License, which permits use, distribution and reproduction in any medium, provided the original work is properly cited.

© 2020 The Authors. *The Depositional Record* published by John Wiley & Sons Ltd on behalf of International Association of Sedimentologists.

palaeo-environmental interpretations of fossil bioherms and phylloid algal mounds on geological timescales.

KEYWORDS

algae, annulate, antecedent, geomorphology, reticulate, self-organisation

1 | INTRODUCTION

Halimeda macroalgal bioherms are a well-recognized biogenic carbonate mound facies in tropical continental shelf-edge and platform-top settings, and contribute an important but poorly constrained component of the neritic carbonate factory (Milliman, 1993; Freile *et al.*, 1995; Hillis, 1997; Rees *et al.*, 2007). In modern reef settings, *Halimeda* is a major contributor to the tropical back-reef carbonate facies (Maxwell, 1973; Orme *et al.*, 1978; Ginsburg *et al.*, 1991; Freile *et al.*, 1995; Hopley *et al.*, 2007), generating aragonite sediments by shedding mature segments as part of its growth-senescence cycle, and seasonally when the thallus dies after producing gametes (Hillis-Colinvaux, 1980; Clifton, 1997). Disaggregated skeletal *Halimeda* segments comprised of calcium carbonate can accumulate as thick mound-like structures (bioherms) over millennial time scales. Modern *Halimeda* bioherms are interpreted as representing a living analogue of their fossil counterparts from the late Miocene (Braga *et al.*, 1996; Martin *et al.*, 1997; Bosellini *et al.*, 2002), and have been compared to the phylloid algal mounds from the Late Palaeozoic (Wray, 1977; Drew and Abel, 1985; Marshall and Davies, 1988; Kirkland *et al.*, 1993; Drew, 2001). This contribution provides a brief updated review of global studies on *Halimeda* bioherms, and presents a new perspective of Modern *Halimeda* bioherm geomorphology that may also have relevance to studies of fossil biogenic carbonate mounds throughout the geological past.

1.1 | Historical studies on *Halimeda* bioherms

The calcareous green macroalgae *Halimeda* originated in the Cretaceous, contributing to reef sediments for at least the last 65 Myr (Elliott, 1965; Hillis-Colinvaux, 1980; Hillis, 1997; 2001), whilst various ‘Halimedeform’ organisms are known from the Jurassic (Elliott, 1965; Hillis, 1997). The significance of *Halimeda* in tropical carbonate sediment production and reef development has been documented for well over a century. In 1887, a geographical expedition to the Solomon Islands identified a fossil reef outcrop described as ‘a true *Halimeda* limestone, entirely composed of joints of *Halimeda opuntia*’ (Guppy, 1887).

The term ‘*Halimeda* bioherm’ was coined by Davies and Marshall (1985) and Orme (1985) to describe the extensive

Halimeda-dominated carbonate mounds in the northern Great Barrier Reef (GBR). Davies (2011), provides a comprehensive discussion on the various terminology used to describe these features (mounds, banks, biostromes, bioherms, reefs and meadows). The term ‘bioherm’, adopted by Davies and Marshall (1985) from the geological definition coined by Cumings (1932), is used here to describe bedded and non-bedded lenticular or mound-like accumulations of in-situ invertebrate organisms with topographic relief above the surrounding seafloor (Davies, 2011). *Halimeda* is not an invertebrate, but a calcareous green alga from the phylum Chlorophyta, order Bryopsidales that produces and sheds aragonitic skeletal grains. In this sense, modern and fossil *Halimeda* bioherms are comparable in lithology, structure and morphology to the aragonitic phylloid algal mounds of the Late Palaeozoic (Wray, 1977; Drew, 1983; Drew and Abel, 1988; Kirkland *et al.*, 1993; Purkis *et al.*, 2015), although taxonomically unrelated.

Modern actively accreting *Halimeda* bioherms are associated with living *Halimeda* meadows, and this highlights the subtle differences in discipline-related terminology. To clarify how these terms have been applied here, *Halimeda* meadows are a thin veneer of living shrubby algae, 10–30 cm high, occurring in dense or patchy carpets (meadows) at the sediment-water interface of the inter-reefal seafloor (Figure 1). The term *Halimeda* meadow is commonly used by biologists, ecologists and phycologists to describe this algal community and benthic habitat. Meadow-forming algae are psammophytic (sand dwelling) with a fleshy holdfast that anchors the plant in soft unconsolidated sediment (Hillis-Colinvaux, 1980). In contrast, lithophytic, or rock-dwelling species of *Halimeda* preferentially attach to hard substrates (Hillis-Colinvaux, 1980; Hillis, 1988) and are common on coralgal reef facies. Both types shed aragonite segments prolifically and are major contributors to reefal sediments, but only the psammophytic species construct bioherms. While modern, actively accreting bioherms are always overlain by a living *Halimeda* meadow, not all meadows are necessarily underlain by a bioherm complex (Hillis, 1988).

1.2 | Global Holocene *Halimeda* bioherms

Halimeda bioherms gained considerable scientific attention from geologists in the late 1970s to 1980s when seismic

and sedimentological surveys in the GBR, Indonesia and the Caribbean first revealed their surface topography and internal architecture. Descriptions of Holocene *Halimeda* bioherms come from the GBR (Davies and Marshall, 1985; Orme, 1985; Drew and Abel, 1988; Marshall and Davies, 1988; Orme and Salama, 1988; Searle and Flood, 1988);

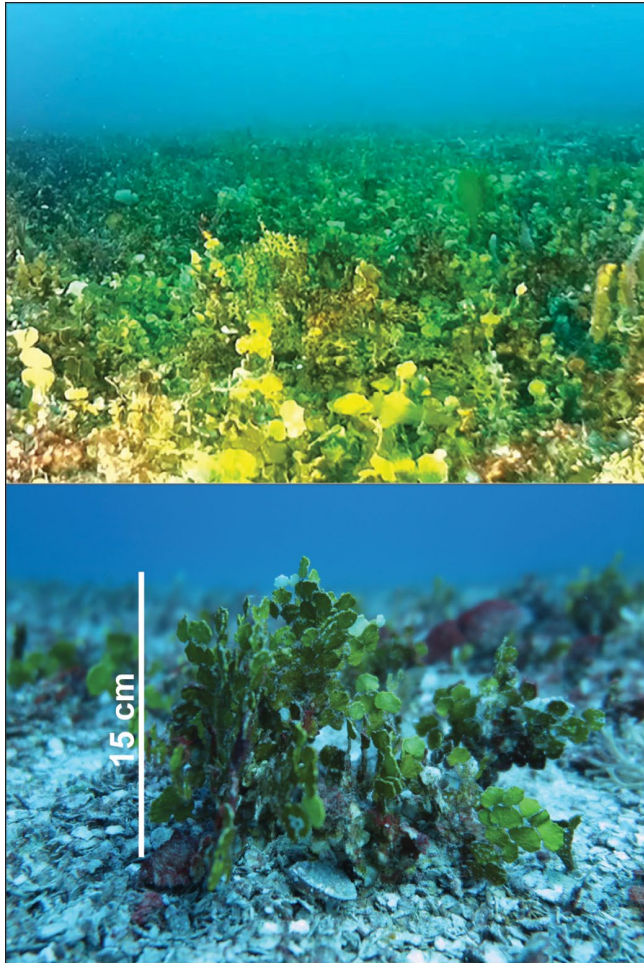


FIGURE 1 Photographs of a living *Halimeda* meadow near Lizard Island in the northern Great Barrier Reef (GBR) (see Figure 3). Photo credit (top) M. McNeil and (bottom) E. Kennedy

Kalukulukuang Bank (K-Bank), Indonesia (Roberts *et al.*, 1987; 1988; Phipps and Roberts, 1988); Miskito Channel in the Nicaraguan Rise, south-west Caribbean Sea (Hine *et al.*, 1988); and reported but not described in detail at Big Bank Shoals on the Sahul Shelf, Timor Sea (Heyward *et al.*, 1997) (Figure 2; Table 1). On the bioherm tops, the seabed is consistently around 20–40 m depth, although the Miskito Channel bioherms are deeper at 40–50 m (Hine *et al.*, 1988). The build-up of *Halimeda* sediment can be up to 50 m thick at K-Bank (Roberts *et al.*, 1988), but 10–30 m thickness is more common at other locations. These bioherm sites are all located on shelf-edge or platform-top positions, with a steep near-vertical slope dropping to an oceanic trough or basin around 1,000 m deep (Table 1). A common interpretation of formation involves the upwelling of cool, nutrient-rich water from below the oceanic thermocline delivering the volume of nutrients required to fuel *Halimeda* growth, not otherwise available from the oligotrophic tropical waters (Wolanski *et al.*, 1988). These consistent characteristics make modern *Halimeda* bioherms an important analogue for the depositional environment, facies interpretation and processes of formation of lithified fossil *Halimeda* deposits (discussed in the following section), and potentially phylloid algal mounds, from the geological past.

1.3 | Global fossil *Halimeda* outcrops

Globally, several fossil *Halimeda* bioherm outcrops have been identified and described (Figure 2; Table 2). The oldest reported example dates back to the Palaeocene and may be the earliest expression of a metre-scale *Halimeda* limestone deposit since this genus first appeared in the Cretaceous. Dragastan and Herbig (2007) describe Palaeocene and Eocene carbonate ramp deposits from the Atlas Mountains (Morocco), comprised almost exclusively of well-preserved *Halimeda* segments. Largely a fossil taxonomic study, the authors do not describe any mound-shaped geomorphology, and so stop short of naming these outcrops as *Halimeda*

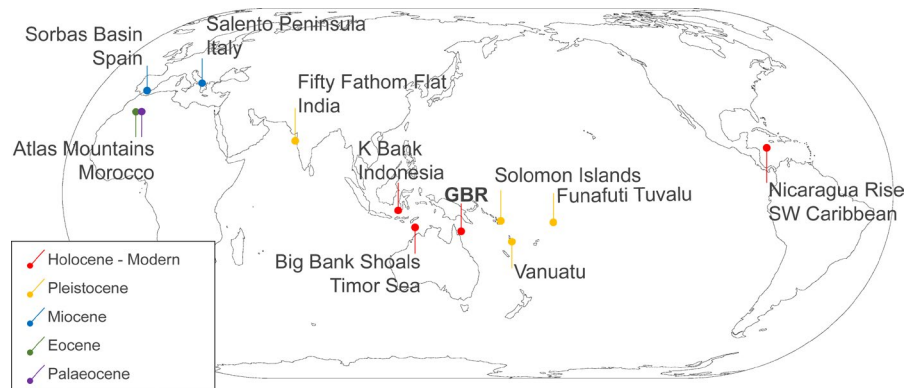


FIGURE 2 Global distribution of known Holocene and fossil *Halimeda* bioherm locations (see Tables 1 and 2). GBR, Great Barrier Reef

TABLE 1 Summary of Holocene/modern *Halimeda* bioherm sites and basic descriptions of geomorphology^a

Location	Depth to mound tops (m)	Adjacent basin depth (m)	Morphology descriptions	Data type	Area (km ²)	Thickness (m)	Reference
Kalukalukuang Bank (K-Bank) Eastern Java Sea, Indonesia	20–40	Strait of Makassar, 800–1,000 m, near-vertical slope edge, thermocline <i>ca</i> 70 m	Elongate ridges and valleys, to hummocky mounds 10–30 m across, to broad undulating areas	Singlebeam echosounder, Reflection seismic	Not quantified	20–50	Roberts, Phipps and Effendi (1987); Phipps and Roberts, (1988); Roberts, Aharon and Phipps (1988)
Nicaraguan Rise, Miskito Channel, South-west Caribbean	40–50	Cayman trough 1,000 m	Mounds with lens-like geometry	Singlebeam echosounder, Reflection seismic	Not quantified	20–30, max 140	Hine <i>et al.</i> (1988)
Big Bank Shoals, Timor Sea, Australia	28–45	300 m depth to base of shoal	Distinct hummocks, less than 150 m across	Bathymetry-method not described, Side-scan sonar	Not quantified		Heyward, Pinceratto and Smith (1997)
Northern Great Barrier Reef, Australia	20–40	Queensland Trough 1–2,000 m, thermocline <i>ca</i> 80 m	Three morphological sub-types: Annulate, smooth ring-shaped mounds; Reticulate high relief non-circular crests; Undulate low relief, smooth sinuous to wave-like	Multibeam echosounder, LADS ^b , LiDAR, Topas sub-bottom profiler, Singlebeam echosounder, Reflection seismic	>6,095	5–20	Orme <i>et al.</i> (1978); Davies and Marshall (1985); Drew and Abel (1985); Orme, (1985); Drew and Abel, (1988); Marshall and Davies (1988); Orme and Salama (1988); Davies (2011); McNeil <i>et al.</i> (2016)
Swain Reefs, southern Great Barrier Reef, Australia	20–30	Capricorn Channel 1–3,000 m in Cato Trough	Morphology not described	Reflection seismic	>70	Up to 14	Searle and Flood (1988)

^aAdapted from McNeil *et al.* (2016).

^bLaser airborne depth sounding.

bioherms. However, they do make an analogous comparison to the modern GBR bioherms.

Perhaps the most spectacular and recognizable lithified fossil *Halimeda* bioherm deposits are those from the upper Miocene in the Sorbas Basin (Spain) (Braga *et al.*, 1996; Martin *et al.*, 1997), and second from Salento Peninsula (Southern Italy) (Bosellini *et al.*, 2002). The lithology and geometry at these two sites are both described as in-situ mid-slope *Halimeda* packstones to floatstones/rudstones, comprising 80%–90% *Halimeda* segments in a carbonate mud matrix, forming discrete lenticular mounds and associated with underlying or adjacent *Porites* coral reefs. In the Sorbas Basin, Braga *et al.* (1996) describe mounds up to 40 m thick and 400 m long, suggesting that these deposits were at least as large, if not larger, than the modern examples of individual

mound structures from the GBR and Indonesia. The coral reef facies association is remarkably similar to modern settings. The erosional discontinuity between the *Porites* reef and *Halimeda* bioherms described from Sorbas Basin is directly analogous to the GBR example, where Holocene *Halimeda* bioherms overly a Late Pleistocene sea-level lowstand erosional unconformity. The GBR underlying Pleistocene surface (antecedent substrate from herein) is comprised of a leached corallgal skeletal packstone/grainstone (Davies and Marshall, 1985).

In the tropical Indo-Pacific, early geologists described *Halimeda*-rich Pleistocene ‘limestone reef’ outcrops from the Solomon Islands (Guppy, 1887), Funafuti (Tuvalu) (Hinde, 1904) and New Hebrides (Vanuatu) (Chapman and Mawson, 1906), comprised almost entirely of well-preserved *Halimeda*

TABLE 2 Summary of described fossil *Halimeda* bioherms^a/reefs

Location	Age	Description	References
Fifty Fathom Flat, India ^a	Late Quaternary	Drowned carbonate platform, outer continental shelf. <i>Halimeda</i> -rich packstone–grainstone showing vadose diagenesis. Mounds 2–4 m thick and 65–385 m across	Rao <i>et al.</i> (1994); Rao, Mahale and Chakraborty, (2018)
Funafuti, Tuvalu	Pleistocene	Atoll, outer slope setting. Well-preserved <i>Halimeda</i> -rich dredged samples. <i>Halimeda</i> unit up to 24 m thick	Hinde (1904)
Solomon Islands	Pleistocene	‘True <i>Halimeda</i> limestone’, entirely composed of joints (segments) of <i>Halimeda</i> opuntia	Guppy (1887)
Vanuatu	Pliocene? to Pleistocene	<i>Halimeda</i> reef-forming limestones. Dominated by well-preserved <i>Halimeda</i> joints (segments). Quite friable	Chapman and Mawson (1906)
^a Sorbas Basin, Spain	Miocene (Messinian)	Mid-slope, laterally restricted <i>Halimeda</i> bioherms (segment reefs) forming discrete lens-like mounds of parautochthonous <i>Halimeda</i> gravel (floatstone/rudstone fabrics). Up to 40 m thick and 400 m long, <i>Porites</i> reef facies association	Braga, Martín and Riding, (1996); Martín, Braga and Riding (1997)
Salento Peninsula, Southern Italy ^a	Miocene (Messinian)	Mid-slope clinostratified <i>Halimeda</i> bioherms associated with <i>Porites</i> reef facies. Well-preserved massive lenticular <i>Halimeda</i> packstones, 30 m long and 4–5 m thick comprising 80%–90% <i>Halimeda</i> segments. In-situ or at least parautochthonous	Bosellini, Russo and Vescogni (2002)
Atlas Mountains, Morocco	Eocene, Palaeocene	Shallow carbonate ramp. Grainstones, packstones, and rudstones composed almost exclusively of well-preserved <i>Halimeda</i> segments, suggesting autochthonous to parautochthonous source. No mound-shaped accumulations are described, therefore the authors stop short of describing these outcrops as <i>Halimeda</i> bioherms, but do make an analogous comparison to the modern Great Barrier Reef bioherms	Dragastan and Herbig (2007)

^aDescribed by those authors as *Halimeda* bioherms.

segments (Table 2). The Funafuti Atoll coral boring geological expedition was embarked upon to test Darwin’s theory of coral atoll formation (Bonney, 1898). Subsequently, Hinde (1904) described a 24 m thick *Halimeda* packstone unit from Funafuti. Chapman and Mawson (1906) estimated the oldest of the New Hebrides *Halimeda* limestones as possible Pliocene, but details of relative dating methods are not clear from the available records. Late Quaternary low mounds (2–4 m thick) are also described from Fifty Fathom Flat off the western coast of India (Rao *et al.*, 1994; 2018) on what is now a drowned carbonate platform.

1.4 | Geomorphology of the *Halimeda* bioherms of the GBR

The GBR bioherms are the most extensive, actively accumulating *Halimeda* deposits in the world (Whiteway *et al.*, 2013). They form part of the GBR World Heritage Area, and their size and extent contribute to the GBR World Heritage Outstanding Universal Values from a geological and geomorphological perspective. The bioherm complexes extend

over six degrees of latitude from 10°S to 16°S and cover an area greater than 6,000 km² (McNeil *et al.*, 2016) (Figure 3). Their calcium carbonate volume is estimated to be up to four times greater than that of the adjacent Holocene coral reefs (Rees *et al.*, 2007). In addition to the expansive northern GBR bioherms, a much smaller area with the same topographic expression has been identified in the southern GBR Swain Reefs region (Searle and Flood, 1988; McNeil *et al.*, 2016) (Figure 3B). Additionally, seismic profiles (Hinestroza *et al.*, 2014) and dredged samples of *Halimeda* floatstone (Abbey *et al.*, 2011) from submerged (up to 130 m depth) shelf-edge reef terraces suggest evidence of *Halimeda*-rich mound development during Late Pleistocene sea-level oscillations (Abbey *et al.*, 2011; 2013; Hinestroza *et al.*, 2014). In the GBR, the previously known extent and geomorphological descriptions were based on sediment grabs, vibracoring, and widely spaced 2D seismic profiling and singlebeam echosounder profiles (Searle and Flood, 1988; Hopley *et al.*, 2007; Rees *et al.*, 2007; Davies, 2011). The first model of *Halimeda* bioherm morphology was constructed at the time, by a reasonable interpolation between 2D parallel seismic and single-beam echosounder profiles, resulting in the elongate parallel

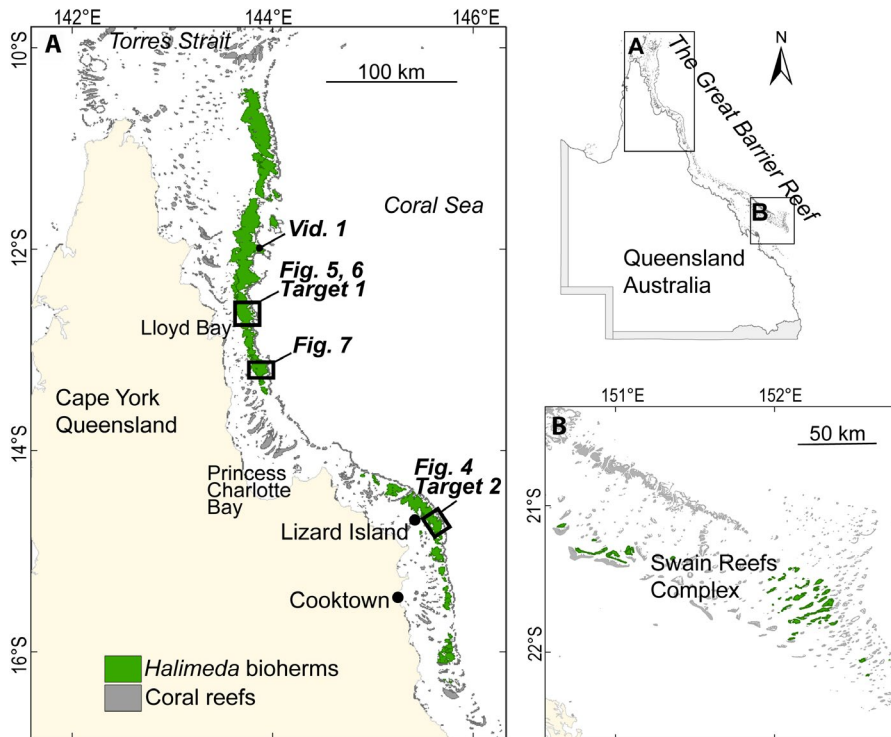


FIGURE 3 Regional map of study area. (A) Northern Great Barrier Reef *Halimeda* bioherm distribution and locations of figures referred to in this study; (B) southern Great Barrier Reef *Halimeda* bioherm distribution in the Swain Reefs. *Halimeda* bioherm distribution from McNeil *et al.* (2016)

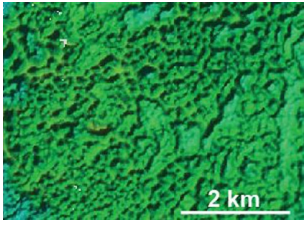
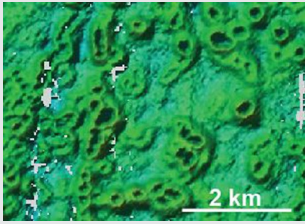
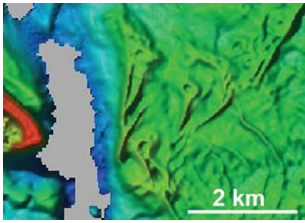
ridges and troughs, and lenticular mound-like morphology descriptions that permeated the literature (Orme and Salama, 1988; Mathews *et al.*, 2007). Previously proposed mechanisms to explain the GBR bioherm morphology include the merging of smaller individual lens-shaped mounds (Marshall and Davies, 1988; Searle and Flood, 1988); stabilization of in-situ accumulations by trapping and baffling by surface flora (Marshall and Davies, 1988); and hydrodynamic processes involving tidal jets and back-reef eddies (Marshall and Davies, 1988; Wolanski *et al.*, 1988). Paradoxically, sediment textural descriptions from core tops suggest little to no winnowing or sorting action by currents (Orme, 1985). Searle and Flood (1988) proposed that bioherm morphology is not inherited from the antecedent substrate based on the planar nature of the underlying surface in the southern GBR.

More recently, descriptions of the spatial distribution and morphology of the bioherms in the northern GBR were re-assessed (McNeil *et al.*, 2016) with the benefit of modern 3D survey technologies such as Laser Airborne Depth Sounding (LADS) bathymetric LiDAR, and multi-beam echosounders (Beaman, 2010). The resulting comprehensive new bathymetry dataset revealed that bioherm shapes and patterns were not consistent with the previous parallel ridges and troughs representation. McNeil *et al.* (2016) identified and described three morphological subtypes, termed reticulate, annulate and undulate (Table 3). The reticulate morphotype has a complex honeycomb-like topography reminiscent of coral patch reef morphology, sometimes described as ‘cellular’ reefs (Purkis *et al.*, 2010; Blanchon, 2011; Blakeway and Hamblin, 2015; Schlager and Purkis, 2015). Perhaps the most striking recent

discovery is the annulate morphotype. These ‘mounds’ appear lenticular or lens-like in 2D profile, but in fact form hollow centred circular ring shapes with elevated crests when viewed in 3D (Video S1). Each annulate ring is 250–300 m in diameter from crest to crest. Adjacent rings sometimes coalesce together sharing side walls (McNeil *et al.*, 2016). The reticulate morphotype tends to be distributed towards the eastern (seaward) bioherm boundary, proximal to the adjacent coral barrier reefs and continental shelf edge that lies 3–4 km to the east. The annulate morphotype is situated more distal to the shelf edge, and annulate rings generally increase in size to westward (away from the shelf break). The undulate morphotype has lower relief, is smoother and more sinuous, and grades into and around the reticulate and annulate types (McNeil *et al.*, 2016). The true nature of bioherm topographical and morphological expression is only revealed when viewed in 3D, and is consistent throughout the entire >6,000 km² distribution.

The recent discovery that the bioherms are much more extensive and morphologically complex than previously thought requires a re-evaluation of existing models describing their origin, growth and development (McNeil *et al.*, 2016). In particular, the processes (e.g. depositional, erosional, hydrodynamic, biological) driving the development of this unusual geomorphology are not understood. It is not clear how the three different morphotypes are developed, particularly the circular annulate rings, although McNeil *et al.* (2016) postulated that biotic self-organization may play a role. Geomorphological differences between the three types, their relationships spatially, and with the underlying antecedent topography have not been assessed. Any future

TABLE 3 Morphological nomenclature, morphotype descriptions and spatial distribution^a

Morphotype	Description	Spatial distribution	Type example
Reticulate	High relief, irregular sharp sinuous crests, complex honeycomb rugosity, non-circular	Proximal to reef and shelf break to east, grading into annulate morphotype	
Annulate	Circular ring shapes, hollow centered with or without central pinnacle, often coalescing together	More distal to reefs and shelf break, generally increasing in size westward	
Undulate	Sinuous and wave-like, smooth crests, with low relief above surrounding sediment	Between and around annulate and reticulate morphotypes, grading into surrounding inter- reef sediment	

^aAdapted from McNeil *et al.* (2016).

analysis of morphological control mechanisms first requires a comprehensive understanding of the physical characteristics of each morphotype.

This study presents a quantitative geomorphological analysis of three different *Halimeda* bioherm morphotypes by integrating the most recently available geophysical datasets to address three main objectives: (a) Combine high-resolution 3D surface bathymetry with co-located acoustic sub-bottom profiles and GIS spatial and morphometric terrain analyses; (b) Quantify the variation in physical characteristics such as bioherm area, thickness, volume and terrain patterns for the annulate, reticulate and undulate morphotypes; (c) Better constrain the size of the *Halimeda* bioherm carbonate factory by quantifying the mass and volume of accumulated CaCO₃ by each morphotype; and (d) Use these analyses to determine the differences and similarities between the annulate, reticulate and undulate morphotypes, and resolve their sedimentological relationships. These analyses will provide crucial new information towards understanding the mechanisms controlling bioherm morphology and potential for biological self-organization.

2 | DATA AND METHODS

2.1 | Surface geomorphic analysis

A GIS geomorphometric analysis was undertaken on the most recently available bathymetric digital elevation model

(DEM) of the northern GBR, that was compiled as part of Project 3D-GBR (Beaman, 2010; 2017) and available for download from the AusSeabed Marine Data Discovery portal (<http://marine.ga.gov.au/#/>). The input datasets used in this study are described in Table S1, with links to open access data repositories where available. The bathymetric DEM is a compiled dataset from all available multibeam echosounder data within the GBR from numerous scientific research voyages, and hydrographic surveys including airborne bathymetric LiDAR acquired by the Australian Hydrographic Office (AHO). The source bathymetry data were collected using a WGS84 horizontal datum and lowest astronomical tide (LAT) vertical datum, with point spacing varying between 6 and 30 m depending on the survey method. A vertical adjustment between LAT and MSL (mean sea level) was made to give an approximate MSL vertical datum across the dataset. The compiled DEM was generated with a 0.0003 arc degree (30 m) pixel size, and then converted to an ESRI raster grid (Beaman, 2017) for spatial analysis in ArcGIS 10.5 software.

This study concentrates on the *Halimeda* bioherm complexes in the northern GBR (Figure 3A). A small area of bioherms is present in the Swain Reefs complex in the southern GBR (Figure 3B). However, mapping in this region is incomplete and the much larger northern section provides a statistically more robust dataset. The distribution of the *Halimeda* bioherm boundaries and delineation of the three morphotypes (reticulate, annulate and undulate) as GIS shapefiles are from McNeil *et al.* (2016).

2.2 | Morphometric analysis

From the >6,000 km² bioherm distribution, two target areas of interest (Figure 3) were selected for detailed analysis that met the following criteria: the area is mapped by a single survey type (the LADS LiDAR bathymetry) for consistency of resolution from the original point data imported to the compiled DEM; covering the largest available area of all three morphotypes; and crossed by Topas sub-bottom profiles running normal (E–W) and parallel (N–S) to the shelf edge (see Section 2.3). Using the 3D Analyst toolbox and Benthic Terrain Modeler (BTM) extensions in ESRI ArcGIS 10.5 with the gridded bathymetry DEM as input data, a set of morphometric derivative outputs were generated to visualize, describe, quantify and compare the surface characteristics across a bioherm complex. These types of terrain attributes can link to physical and biological explanatory processes (Lecours *et al.*, 2016; Walbridge *et al.*, 2018). The geomorphometry derivatives presented in this study for target area 1 (e.g. slope, aspect, curvature, terrain ruggedness.) are comprehensively described by Walbridge *et al.* (2018), with mathematical algorithms and extended references, including their workflow through the ArcGIS BTM software. These methods, and the context to which they have been applied, are briefly described herein.

Surface gradients (slope, aspect, curvature) calculated from the pixel–pixel relationships in bathymetric data form the foundation of the morphometric analyses (Lecours *et al.*, 2016). Two slope derivatives are presented, one on the planar cartesian surface and an arc slope calculated on the geodesic ellipsoid. The arc slope method accounts for the angle between the input surface and the geodetic datum, applies a least squares fitting, and can produce more accurate results when applied to high resolution bathymetry with low positional uncertainty (Passalacqua *et al.*, 2015). The two slope outputs are displayed with different symbology to highlight features of interest. To compare the annulate morphotype inner slope gradient with the outer slope gradient, a subset of annular rings were manually selected within target area 1 and used to calculate the average slope. The largest six rings were selected because larger rings are represented by a greater number of pixels ($n = 206$ pixels). Rings were cross-checked against the aspect azimuth to confirm inward-facing from outward-facing pixels, then the slope gradient for each inward and outward-facing pixel was recorded. Profile curvature calculates the change in slope across bioherm features and the adjacent non-bioherm seafloor. Application of the aspect computation generates a statistical visualization of surface direction, or ‘easterness’ and ‘northernness’ (Walbridge *et al.*, 2018) in azimuth degrees for each cell.

Bathymetric position index (BPI) is a measure of relative position (elevation) between any cell and the overall seascape, by computing the difference between any cell

and the mean elevation of all cells within a surrounding annulus-shaped neighbourhood (Lundblad *et al.*, 2006). Usually computed over both broad and fine scales, only the broad-scale BPI is presented as this provided the most appropriate scale from the input data resolution and the size of the target area of interest. The default neighbourhood radii values of one and three pixels were used for the inner and outer annulus circles respectively. Resulting values are positive near crests and ridges, and negative near depressions and valley bottoms.

The ArcGIS BTM provides four methods across three tools to quantify terrain complexity or surface heterogeneity: Surface Area to Planar Area (SAPA) and slope corrected SAPA, Vector Ruggedness Measure (VRM) (previously termed Rugosity in BTM), and Arc-chord ratio. The VRM described by Sappington, Longshore and Thompson (2007) was applied in this analysis. The VRM calculates a dimensionless metric of terrain complexity using a moving 3×3 cell window, where values range from 0 (no terrain variation) to 1 (complete variation) (Walbridge *et al.*, 2018). All of these geomorphometric outputs and numeric derivatives are scale and resolution dependent, and the process of creating the input DEM surface (30 m gridded resolution) will affect the accuracy and error margin of the outputs. For example, a single annulate ring of 300 m diameter would be covered by a grid of 10×10 pixels. A 3×3 cell window in the BTM morphometry computations was found to be the most appropriate scale for the input data.

2.3 | Subsurface geomorphic analysis

Subsurface acoustic data were collected using a Kongsberg TOPAS PS-18 sub-bottom profiler (frequency 1,000 to 6,000 Hz, 1,500 Hz central frequency) on the RV *Southern Surveyor* voyage SS09/2008 (Tilbrook and Matear, 2008). Over 210 km of seismic data in seg format were viewed in IHS Markit Kingdom seismic interpretation software (2017 version). To calculate the *Halimeda* bioherm thickness, the seafloor horizon (bioherm top surface) and the first prominent seismic reflector (bioherm bottom surface) were delineated. This first reflector was termed Reflector A following the notation of Orme *et al.* (1985) who interpreted this reflector as the Pleistocene erosional unconformity that marks the antecedent substrate of the Holocene *Halimeda* bioherms. Reflector A was delineated using a combination of automated and manual horizon picking to avoid interpreting multiples (seismic artefacts). The isochron thickness between these two horizons was then computed in two-way travel time (TWT; ms) with these xyz data exported as a text file. The isochron xyz data were imported into ArcGIS and clipped using the *Halimeda* bioherm shapefile extent (McNeil *et al.*, 2016), to ensure that only areas confidently

identified as *Halimeda* bioherms were included in subsequent calculations. To reduce the margin of error of the thickness calculation, any discontinuous or uncertain sections of Reflector A were excluded from the dataset, such that the isochron thickness, and subsequently the bioherm volume, was only calculated on sections where Reflector A could be confidently delineated.

Statistical calculations (ANOVA) of the differences in thickness between the reticulate, annulate and undulate morphotypes were calculated on TWT. To present a meaningful description of thickness and for use in bioherm volume calculations, TWT was converted to an estimate of thickness in metres by applying the best estimate of *Halimeda* sediment acoustic velocity from the literature. Skjold (1988) undertook a continuous seismic reflection (boomer, dominant frequency 3–4 kHz) and vibracoring survey close to the target area of interest 1. The seismic acoustic parameters and sediment physical properties from that survey are compiled in Table 4. Average acoustic velocity in the *Halimeda* lithofacies is $1,532 \pm 19$ m/s ($\pm SE$) calculated from 24 measurements across five *Halimeda* vibracores. These short cores (max 3.8 m) only capture the top section of the full bioherm sequence. Therefore, acoustic velocity may vary downcore with increased compaction or changes in sediment texture. However, these are the only seismic velocity data currently available for any GBR survey that specifically targets *Halimeda* bioherms, and are consistent with the summary of carbonate Quaternary P-velocities summarized by Hinestrosa *et al.* (2014). The bioherm volume (km^3) was calculated for each morphotype by multiplying average thickness of each morphotype (m) by planar area (m^2) and converting to km^3 . Furthermore, the grain density, porosity and $\text{CaCO}_3\%$ measured by Skjold (1988) (Table 4) were used to calculate the volume and mass of CaCO_3 by each morphotype by adapting the equations described in Rees *et al.* (2007).

$$\text{Bioherm volume } V_b = T_b \times A_b$$

$$\text{CaCO}_3 \text{ volume } V_c = V_b \times [1 - \emptyset] \times C$$

$$\text{CaCO}_3 \text{ mass } M_c = V_c \times \rho$$

where V = volume (m^3), T = thickness (m), A = planar area (m^2), \emptyset = porosity, C = $\text{CaCO}_3\%$, and ρ = grain density (*Halimeda* aragonite g/cm^3). Results were converted to km^3 and Gt for volume and mass respectively.

Statistical analyses to compare differences in measured morphometric parameters between the annulate, reticulate and undulate morphotypes were undertaken by analysis of variance (Kruskal–Wallis one-way ANOVA). The H -statistic tested the hypothesis of no statistically significant difference in median values between the three morphotypes.

3 | RESULTS

3.1 | Surface geomorphometry and quantitative morphometrics

Results presented here are from two representative target areas of *Halimeda* bioherm morphology that express the topography and spatial organization of the three morphotypes, annulate, reticulate and undulate, from over 210 km of sub-bottom profiles combined with high-resolution LiDAR bathymetry.

The annulate morphology is characterized by sedimentary packages with high positive relief that are relatively uniform in thickness except where punctuated by annular rings. The central hollow of the rings plunge to the deepest section, at times almost reaching the antecedent substrate (Figure 4A). The annulate surface is sinuous and relatively smooth between individual rings, compared with the reticulate surface (Figure 4C). The crests of each ring are gently convexly curved, and the inward-facing slope is consistently steeper than the outer slope (Figure 4E). Calculations based on the ArcGIS BTM outputs indicate that the inner slope gradient is approximately three times steeper than the outer slope (Table S2 and Figure 5C). The antecedent substrate (Reflector A) is prominent and some internal bedding is evident in the bioherm. The topmost internal bedding reflectors are generally parallel to sub-parallel to the seafloor, following the upwardly convex curvature of the mounded surfaces, and generally downlapping on underlying surfaces. These internal reflectors are indicating metre-scale features and it is not entirely certain what this bedding represents.

The reticulate morphology (Figure 4C) is considerably more complex, with steeper topographic relief and sharper crests than the annulate rings. There is more variability in bioherm thickness, but the valleys and depressions seldom reach the antecedent substrate. The internal reflectors are also more complicated, at times showing the convex-up bedding similar to the annulate morphotype, but also showing evidence of abrupt truncations (e.g., Figure 4D), and multiple generations of growth or deposition.

The undulate morphotype (Figure 4B) typically shows very little topographic relief. The surface is smooth to wavy, and internal bedding is parallel to both the seabed and antecedent substrate. There are two prominent ‘basement’ reflectors in the seismic section presented in Figure 4B. It is not certain whether the first prominent reflector is an internal bedding surface and the second reflector is Reflector A (Holocene/Pleistocene boundary), or whether the first reflector is Reflector A and the second is a pre-Holocene surface. The paucity of available core material limits cross-referencing of seismic stratigraphic features against lithostratigraphy in most areas.

TABLE 4 Physical properties of five *Halimeda* sediment vibracores, ca 3 m long, from Lloyd Bay northern Great Barrier Reef (Figure 3). Acoustic data were derived from a continuous seismic reflection survey (boomer, 3–4 kHz dominant frequency; Orme, 1985; Orme and Salama, 1988; Skjold 1988). Sediment physical properties were determined by gravimetric methods detailed in Skjold (1988)

Core	Seq	Length (m)	Acoustic velocity (m/s)	Lith	Z (A. Imp.)	Bulk density (g/cm ³)	Grain density (g/cm ³)	Water (%)	Porosity, ϕ (%)	CaCO ₃ (%)	Compact. (%)
137	11	0.62	1,527	4	2,522,627	1.65	2.72	39	63	91	20
137	11	1.24	1,616	4	2,491,655	1.54	2.38	41	62	87	20
137	21	1.86	1,577	4	2,960,795	1.88	2.72	27	50	97	20
137	21	2.48	1,617	4	2,633,115	1.63	2.43	36	57	91	20
137	21	3.1	1,545	4	2,736,387	1.77	2.74	33	56	91	20
137	21	3.73	1,493	4	2,488,038	1.67	2.77	39	63	67	20
156	1	0.56	1,469	4	2,551,800	1.74	2.91	37	62	96	11
156	1	1.13	1,439	4	2,309,113	1.61	2.76	43	67	88	11
156	1	1.69	1,473	4	2,578,550	1.75	2.73	34	57	97	11
156	11	2.14	1,450	4	2,639,358	1.82	2.92	33	58	98	11
196	1	0.64	1,535	4	3,222,373	2.1	2.68	17	35	92	22
196	31	1.29	1,503	4	2,586,312	1.72	2.86	37	62	79	22
196	31	1.93	1,503	4	2,556,539	1.7	2.88	38	64	80	22
196	31	2.57	1,540	4	2,533,002	1.65	2.94	42	68	88	22
196	75	3.2	1,921	6	4,068,329	2.12	2.87	20	41	94	22
207	1	1.02	1,519	4	3,398,830	2.24	2.8	15	32	100	0
207	11	1.53	1,536	4	2,620,119	1.71	2.77	37	61	99	0
207	11	2.05	1,557	4	2,600,704	1.67	2.75	38	63	98	0
207	11	2.55	1,543	4	2,677,409	1.74	2.83	36	61	97	0
207	11	3.07	1,538	4	2,702,100	1.76	2.72	33	57	98	0
207	11	3.84	1,494	4	2,481,526	1.66	2.8	40	64	98	0
210	1	1.71	1,445	4	2,219,424	1.54	2.89	48	73	93	0
210	1	2.85	1,463	4	2,347,624	1.61	2.83	43	68	92	0
210	11	2.27	1,486	4	2,409,569	1.62	2.79	42	66	92	0
Mean (\pm SE)			1,532 \pm 19		2,680,637 \pm 80,495	1.75 \pm 0.03	2.77 \pm 0.02		58 \pm 2.06	92 \pm 1.54	

Note: Seq = sequence stratigraphic unit; Lith = lithostratigraphic unit, 4 = *Halimeda* sediment, 6 = limestone/calcrete; Z = acoustic impedance; Compact. = compaction from vibracoring (core barrel penetration vs. measured length of core) (Skjold, 1988).

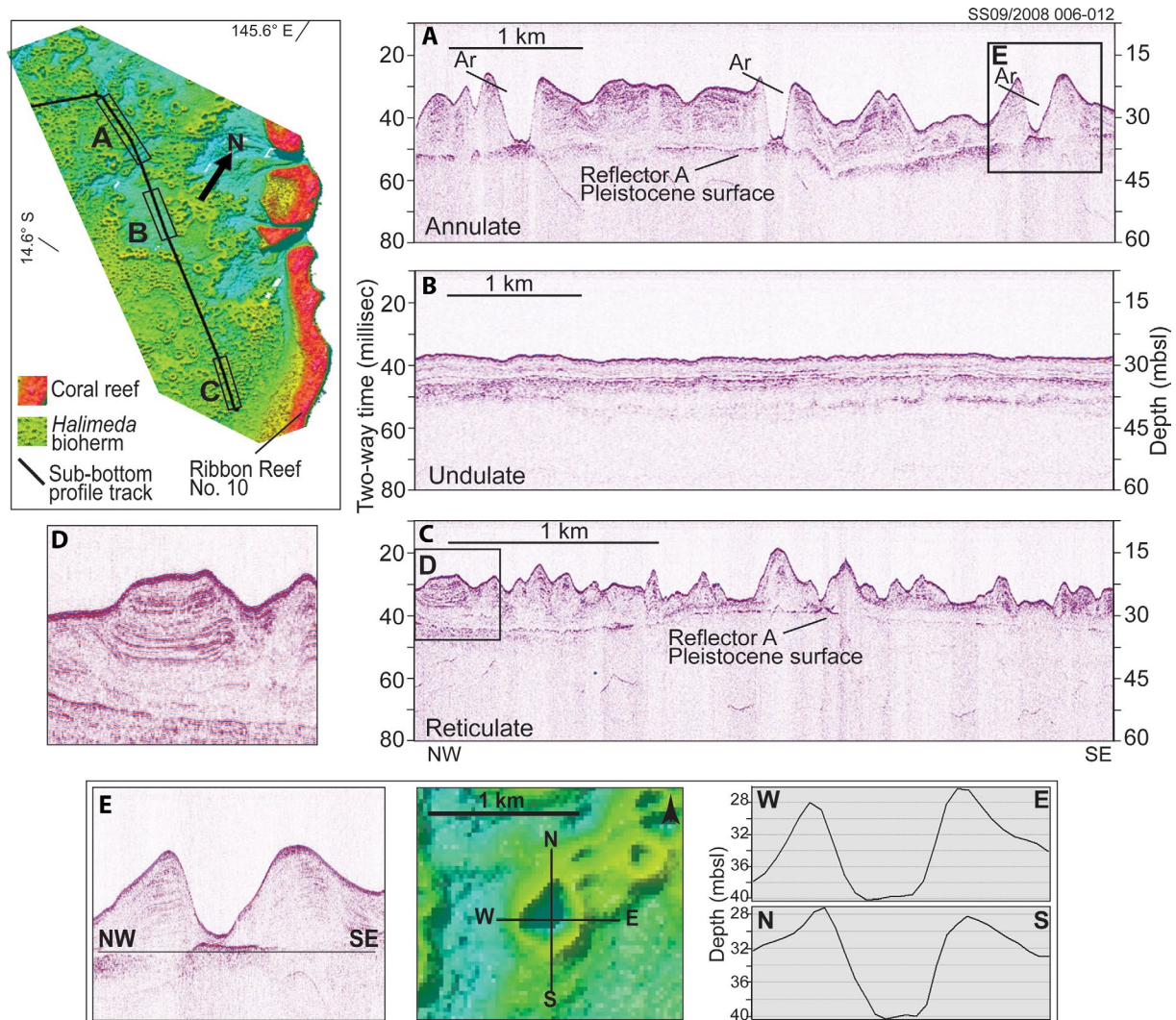


FIGURE 4 Type examples of (A) annulate, (B) reticulate and (C) undulate morphotype sub-bottom profiles showing surface topography and internal sedimentary architecture from Target area 2. See Figure 3 for location. Inset (D) internal reflectors indicate some truncated erosional surfaces in the reticulate morphotype; (E) annulate ring crests and hollow showing proximity to the antecedent substrate and differentiation between inward-facing and outward-facing slope gradients. Ar = annulate ring. Reflector A is interpreted as the Holocene/Pleistocene erosional unconformity (Davies and Marshall, 1985; Orme, 1985; Orme and Salama, 1988). An acoustic velocity of 1,532 m/s (Table 4) was used to convert from time (TWT ms) to depth domain (m below sea level [m.b.s.l.]) on sub-bottom profiles

The results from the ArcGIS BTM geomorphometry analysis (Figure 5) reinforce the heterogeneity observed from 2D seismic profiles, and add further insights to the characteristics of the annulate and reticulate morphotypes. The reticulate morphotype is most common on the eastern (seaward) side of the bioherm complex, proximal to the outer barrier coral ribbon reefs and continental shelf edge and forms the eastern bioherm boundary (Figure 5A). The annulate morphotype lies westward, further from the shelf edge and grading out to the western boundary. Coverage of the undulate morphotype increases to the west, away from the shelf edge. It is organized between and around the other two types, grading out to the surrounding inter-reef sediment.

The bioherm boundary is marked by a clear difference in topographic relief between the bioherm tops and the adjacent outer-shelf seafloor. There is an approximately 30 m difference in bathymetry between the outer-shelf seafloor and the western bioherm boundary (Figure 5B). The tops of both the annulate and reticulate morphotypes are relatively consistent with each other, with the exception of the annulate ring hollows that plunge to the depth of the antecedent substrate. Table 5 shows the combined average bathymetry from target area 1 and target area 2, for each morphotype. The slope output highlights striking differences between the three morphotypes (Figure 5C). First, the annulate rings clearly show a bi-modal slope distribution, expressed as a double ‘halo’ effect. The inner, brighter circle shows the steeper slope of the

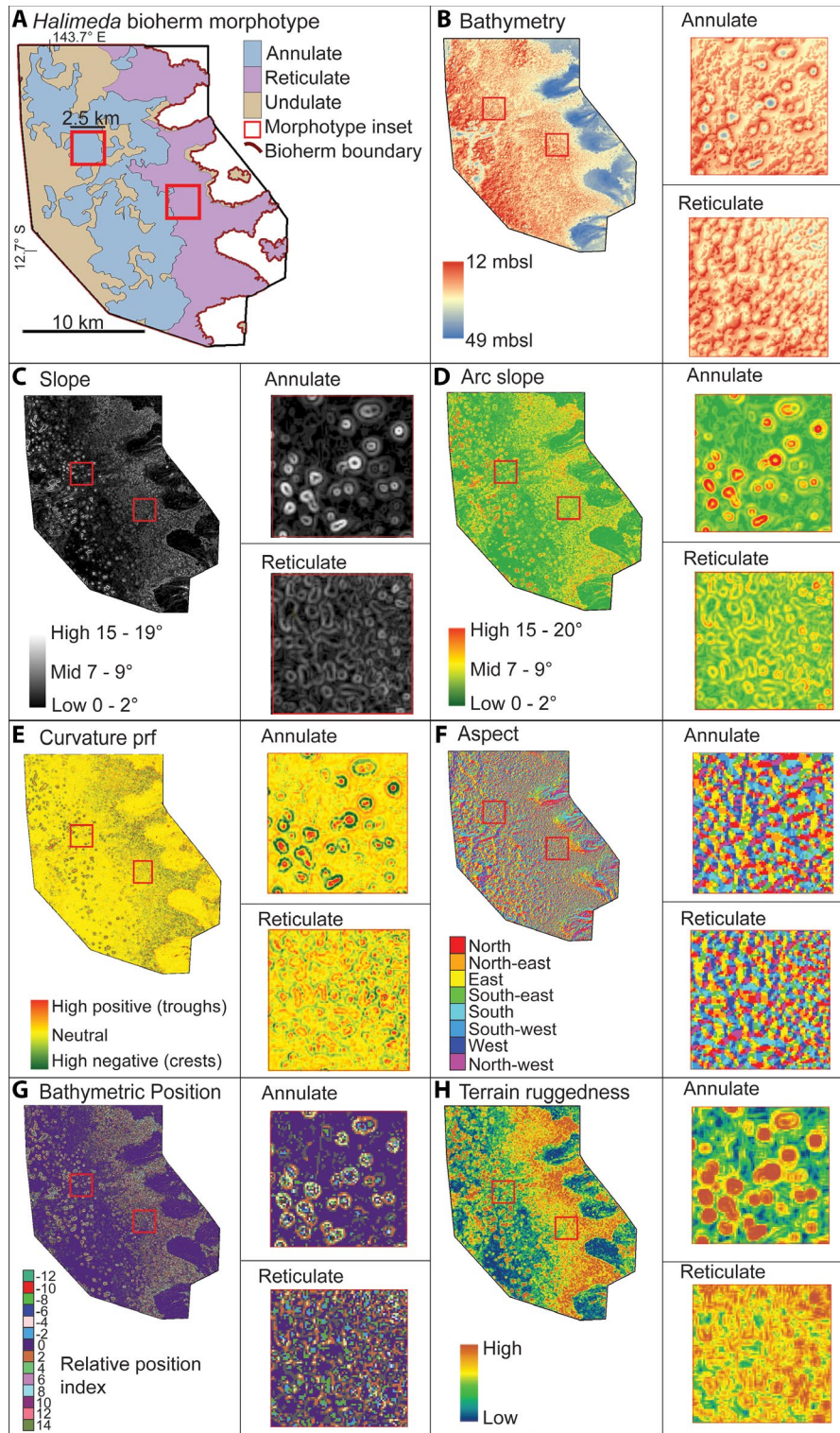


FIGURE 5 Morphotype and morphometric characteristics of area of interest Target area 1 (see Figure 3). Red insets highlight the annulate and reticulate morphotype surface characteristics in a 2.5 km x 2.5 km clip of each type

inward-facing walls and the outer circle shows a more moderate slope on the outward-facing flanks of each annular ring. The total average annulate slope is 1.88° overall (Table 5) but the individual ring outer slope is 2.87° vs the inner slope of 8.92°; the inner slopes are approximately three times steeper

than the outer slopes (Table S2). The low gradient of the annulate ring crests (black circle between the bright inner and outer circles, Figure 5C) illustrates the smooth curvature of the annulate ring crests compared to the much sharper nature of the reticulate crests. The reticulate slope inset (Figure

TABLE 5 Quantitative morphometric summary of surface and subsurface parameters from Target area 1 and 2. Average bathymetry, bioherm thickness, slope and calculated depth from sea level to antecedent substrate (mean \pm SE). Antecedent depth is the sum of average bathymetric depth and average bioherm thickness

	Surface		Subsurface	
	Bathymetry ^a (m.b.s.l.)	Average slope ^b (°)	Thickness ^c (m)	Antecedent depth (m.b.s.l.)
Annulate	24.52 \pm 0.01	1.88	12.69 \pm 0.02	37.21 \pm 0.02
Reticulate	28.64 \pm 0.01	2.71	9.80 \pm 0.02	38.44 \pm 0.02
Undulate	25.67 \pm 0.02	1.38	6.99 \pm 0.03	32.66 \pm 0.04

^aFull bathymetry descriptive statistics for Target area 1 and 2 provided in Table S4.

^bFull slope descriptive statistics and histograms for Target area 1 is provided in Table S3.

^cFull seismic isochron thickness descriptive statistics for SS09/2008 Topas sub-bottom profile track provided in Table S5.

5C,D) highlights the very different surface topography of this morphotype compared to the annulate. Average slope is 2.71° overall (Table 5), steeper than the average annulate gradient, but lacking the double slope expression of the annulate rings. The difference in spatial organization and surface topography between these two morphotypes is remarkable. The coloured symbology of the arc slope morphometry (Figure 5D) displays the same data but highlights: (a) the almost flat gradient of the adjacent shelf-edge seafloor and the undulate morphotype (which has an average slope of 1.38°; Table 5); and (b) the abrupt change in bathymetry is expressed by the steep slope at the bioherm eastern boundary (Figure 5B). This is clearly illustrated in the curvature output, showing the change in slope (Figure 5E). Here, the change in slope (curvature) at the bioherm boundary is very high (coloured red), showing that the topography steepens sharply from the seafloor to the bioherm surface, rather than a gradual gradient.

The aspect morphometry (Figure 5F) illustrates that both the annulate and reticulate azimuth orientations are similarly random in all directions and do not appear to express any preferred orientations in 3D space.

The preceding surface gradient morphometrics combine to form the basis of the overall terrain complexity, illustrated by the VRM and the BPI. The BPI output (Figure 5G) shows the relative differences in elevation between any cell and the surrounding 3 \times 3 neighbourhood, such that the purple areas show neutral BPI and coloured pixels show relative positive and negative bathymetric positions. This result shows that the shelf-edge seafloor and the undulate morphotype share similarly flat terrain relative to the surrounding seascape, even though they are at different bathymetric depths. In contrast, the reticulate morphotype shows irregular and variable BPI compared to the regularly spaced patterning in the annulate morphotype. Similarly, the VRM terrain ruggedness (Figure 5H) further illustrates the topographic complexity of the reticulate morphotype in particular, compared with the annulate and undulate morphotypes. The annulate complexity or ruggedness is pronounced at each individual ring but otherwise is relatively topographically smooth between the rings.

3.2 | Subsurface geomorphometry and quantitative morphometrics

Analysis of the seismic isochron thickness shows significant differences in the bioherm thickness between the three morphotypes (Kruskal–Wallis ANOVA, $p < .001$, Table S6). In summary, the average annulate thickness is 12.69 \pm 0.02 m, reticulate is 9.80 \pm 0.02 m, and undulate is 6.99 \pm 0.03 m (Table 5). These thicknesses were calculated from a time-to-depth conversion based on the average seismic velocity presented in Table 4. The isochron thickness was only calculated where the seismic Reflector A could be confidently delineated, therefore the thickest sediment packages that were too seismically opaque to confidently pick Reflector A are not included in these calculations; these should be considered as minimum thicknesses. By calculating the sum of the bathymetric water depth and bioherm thicknesses the depth to the antecedent substrate was estimated (Table 5). Annulate and reticulate antecedent substrate depths are similar (37.21 \pm 0.02 and 38.44 \pm 0.02 m.b.s.l. respectively), but undulate depth is *ca* 6 m less (32.66 \pm 0.04 m.b.s.l.) as a result of the shallower average bathymetry and less sediment thickness.

Two sub-bottom profiles from target area 1 (A–A' west-east and B–B" north–south) illustrate the typical bioherm topographic relationships with the underlying antecedent substrate (Figure 6). The undulate morphotype (Figure 6A) shows parallel to sub-parallel internal bedding overlying a planar substrate reflector. The eastern edge of Inset a grades into the reticulate morphotype (Figure 6B) showing no apparent change in the planar antecedent substrate. In 2D profile, the reticulate crests and valleys (Figure 6B) do not correspond with any antecedent features. The intersection of profiles A' and B cut across the eastern edge of the *Halimeda* bioherm at a point where the ship track changes direction to north-south. This intersection clearly shows the expression of bioherm surface topography and the prominence of the seafloor and Reflector A at the eastern boundary edge and outer shelf. Reflector A remains planar and the shelf seafloor is covered by a very thin veneer of Holocene sediment. The

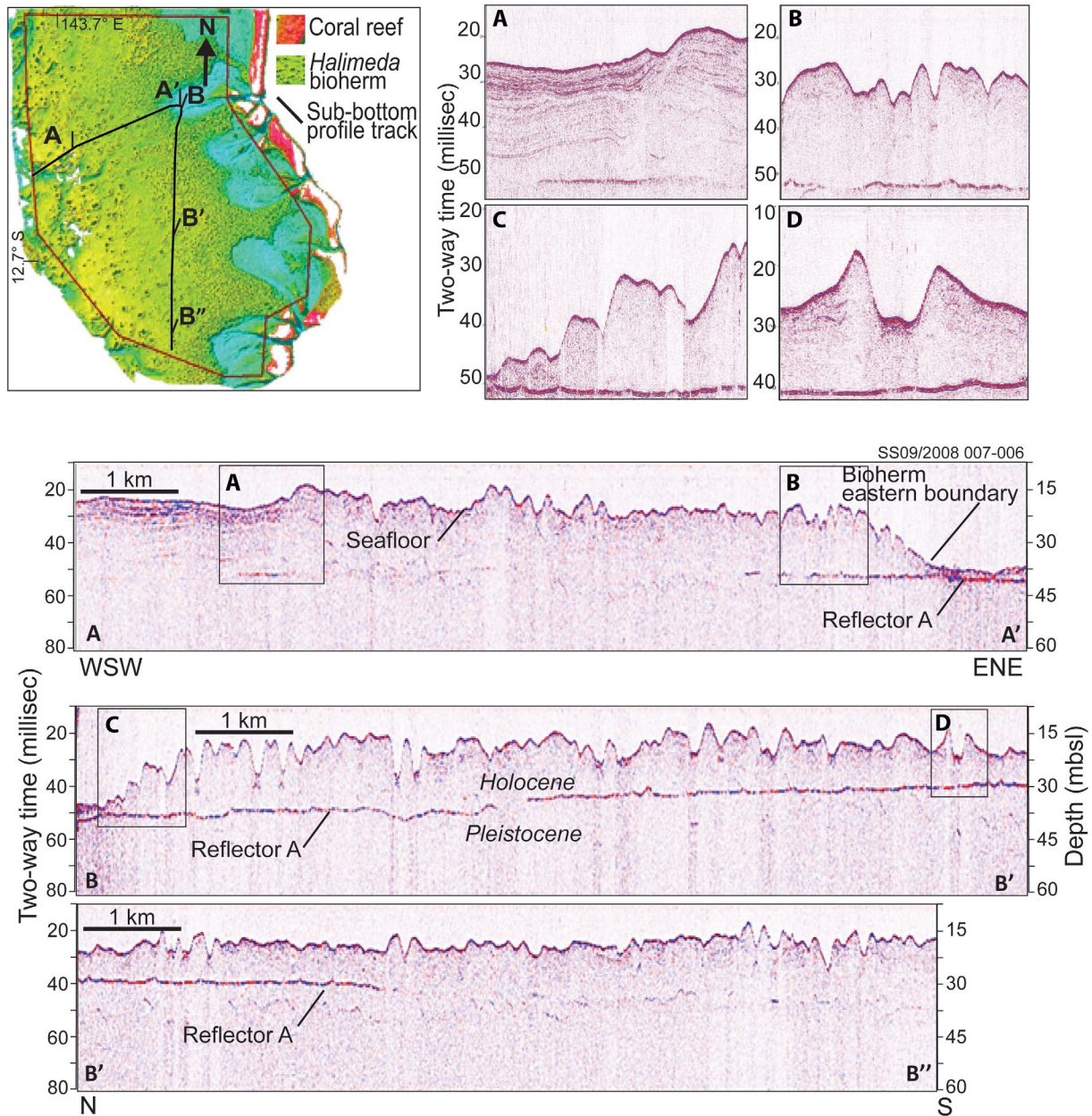


FIGURE 6 Examples of surface profile relationships with antecedent basement topography. Reflector A is interpreted as the Holocene/Pleistocene erosional unconformity (Davies and Marshall, 1985; Orme, 1985; Orme and Salama, 1988). Total sub-bottom profile horizontal distance is approximately 25 km. An acoustic velocity of 1,532 m/s (Table 4) was used to convert from time (TWT ms) to depth domain (m below sea level [m.b.s.l.]) on sub-bottom profiles

reticulate bioherm morphotype again commences at the bioherm edge (B–B', Figure 6C), rising abruptly from 5 to 15 m thick. Figure 6D highlights an annular ring, and the transition from reticulate to annulate also does not correspond with any change in the expression of the antecedent substrate, nor do the crests and hollows of the ring. Profile B–B' and B'–B'' shows a gradual shallowing upwards of Reflector A from 40 to 30 m.b.s.l. running north-south. However, the corresponding bathymetry of the bioherm tops remains relatively uniform at ca 15 m.b.s.l., due to a thinning sediment package over Reflector A, rather than a 10 m shallowing in

bathymetry. The gradual shallowing upwards of Reflector A is a result of the slope geometry of the continental shelf, whereby the top of the profile track at B is proximal to the shelf edge (and hence deeper Reflector A) and B' is more distal from the shelf edge because of the wider shelf here.

The antecedent substrate deviates from planar where the outer shelf is incised by palaeochannels and inter-reef passages. In some sections, submerged coral reefs lie immediately proximal to *Halimeda* bioherms, while in others reef pinnacles protrude through Holocene sediments (Figure 7). Profile A–A' crosses a broad channel and it is assumed that

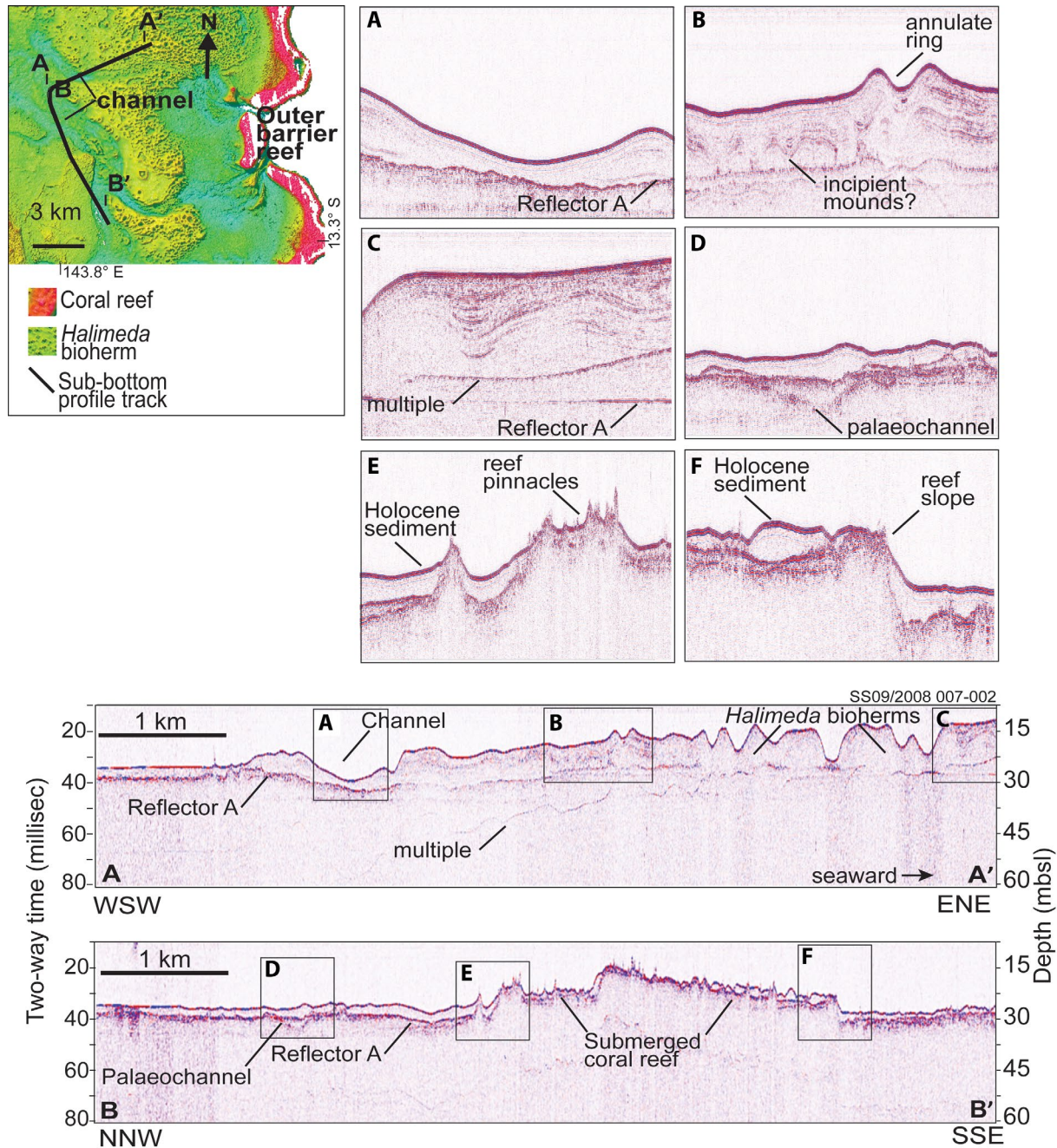


FIGURE 7 Bioherm relationships with adjoining submerged reefs and incised channels showing internal sedimentary architecture and antecedent topography. An acoustic velocity of 1,532 m/s (Table 4) was used to convert from time (TWT ms) to depth domain (m below sea level [m.b.s.l.]) on sub-bottom profiles

the overlying sediment package is *Halimeda*, then continues into a bioherm with undulate to annulate morphology. The channel base highlights the prominent wavy erosional expression of Reflector A, and the overlying sediment is smoothly sinuous with an upwardly convex bedding that grades from parallel with the antecedent substrate, to parallel with the seafloor. The rest of profile A–A' shows the characteristic annulate topography seen in Figure 4A, but some interesting internal features stand out. Figure 7B and C clearly show evidence of incipient mounds accumulating on Reflector A that

are subsequently overlain by younger layers that drape across the low mounds and become parallel to the seafloor. Profile B–B' crosses a broad channel intersected by a submerged coral reef. The channel has a more complicated antecedent substrate than that in Figure 7A, showing two erosional surfaces. There is evidence of overbank deposits either side of the channel, with laterally continuous younger Holocene sediment deposited on top that is truncated by the emergence of a submerged reef pinnacle (Figure 7E). The submerged coral reef shows typical steep slopes and 'spiky' topographic

TABLE 6 Bioherm area and volume, % contribution, and CaCO₃ volume and mass calculations. CaCO₃ volume and mass calculated from measured grain density, porosity and CaCO₃% average values from Skjold (1988; Table 4)

	Planar area (km ²)	Area cont. (%)	Bioherm volume (km ³)	Volume cont. (%)	CaCO ₃ volume (km ³)	CaCO ₃ mass (Gt)
Annulate	935	15	11.87	23	4.59	12.70
Reticulate	1,226	20	12.02	23	4.64	12.86
Undulate	3,949	65	27.61	54	10.67	29.55
Total	6,111	100	51.50	100	19.90	55.12

relief in profile (Figure 7F). Although somewhat mounded (Figure 7F), it is unlikely that the overlying thin Holocene veneer of sediment is in-situ bioherm-forming *Halimeda*, because they favour unconsolidated sediment.

3.3 | The *Halimeda* bioherm carbonate factory

An estimate of the size and volume of the bioherm carbonate factory is obtained from the subsurface calculation of bioherm thickness (Table 6). In total, the bioherms cover an area of 6,111 km² with a total volume of 51.5 km³. Taking into account average porosity, grain density and % CaCO₃, the total contribution of CaCO₃ to the system is 19.9 km³ by volume, and 55.12 Gt by mass (ca 9 M tonnes CaCO₃ km⁻²). The three morphologies differ in their percentage contributions to area and volume respectively (Table 6). The annulate morphotype contributes 15% of the planar area but 23% of the CaCO₃ volume, due to the greater sediment thickness (Table 5). The reticulate morphotype contributes 20% of the area and 23% of the CaCO₃ volume, and the undulate morphotype contributes 65% of the area but 54% of the CaCO₃ volume because the sediment thickness is considerably less than that of the other two morphotypes. The values presented in Table 6 are estimates based on the accuracy and potential sources of uncertainty of the input parameters. The thickness (*T*) is dependent on the accuracy of the seismic velocity time-to-depth conversion, and the grain density, porosity and CaCO₃% parameters are average values. The bioherm area is dependent on the accuracy of the original delineation of their spatial distribution at the 30 m pixel resolution. Nevertheless, these results represent the best available estimate of the size of the *Halimeda* bioherm carbonate factory. There are clear differences in area and volume between the three morphotypes which may be reflecting varying aggradation and progradation dynamics.

4 | DISCUSSION

Prior to 2016, the three different *Halimeda* bioherm morphotypes were unknown, and morphological descriptions

were based on singlebeam echosounder and widely spaced 2D seismic profiles. The dataset is still limited to single lines of 2D sub-bottom profiles, albeit over substantial distances. Crucially, it is now possible to correlate sub-bottom profiles with high-resolution 3D LiDAR bathymetry, allowing the substrate beneath the annulate, reticulate and undulate morphotypes to be explored for the first time. This is a significant advance over previously available data, revealing new insights on the linkages between surface and subsurface geomorphology and similarities and differences in the development of the three morphotypes.

Based on the data available at the time, earlier interpretations of the bioherms described them as a single morphological entity. Some authors recognized a degree of variation, describing that the topographic relief is better developed and more pronounced eastward, with smaller, less complex mounds to westward (Marshall and Davies, 1988; Orme and Salama, 1988). The results presented here provide multiple lines of evidence that the annulate, reticulate and undulate morphotypes are each distinctly different, expressed by their differing geomorphometric characteristics and internal thickness and bedding. These geomorphological differences suggest some degree of heterogeneity between morphotypes with respect to the biotic and/or abiotic mechanisms that modulate their growth and development. First, the differences in physical characteristics between morphotypes based on the BTM morphometric results, and implications for the growth potential of the bioherm carbonate factory are discussed. Second, the subsurface internal architecture and relationships with the pre-Holocene antecedent topography are presented. Third, some biological observations linking living *Halimeda* meadows to sedimentological accretion are introduced. And fourth, the potential for biotic self-organization in mediating *Halimeda* bioherm geomorphology are discussed together with some suggested preliminary hypotheses and methodologies for future studies.

4.1 | Surface morphometry and quantitative metrics

The three morphotypes show significant differences in sediment accumulation (thickness), and in the depth to the

antecedent substrate (Table 5). These metrics equate to vertical accommodation space and growth potential from the pre-Holocene flooding surface. The average depth to the antecedent substrate for annulate and reticulate morphotypes is similar (37.21 ± 0.02 and 38.44 ± 0.02 m.b.s.l. respectively), however, they differ in their average sediment thickness by almost 3 m. Additionally, the undulate morphotype is on average approximately half the thickness of the annulate, but over a much larger area (65% of the distribution). To explain these differences, the three morphotypes must have different growth rates and ability to produce living biomass and therefore sediment accumulation. Or alternatively, if their capacity for growth is the same, then they must be affected by different regimes of sediment redistribution or erosion (deposition). Previous work has established that the three morphotypes have a generalized cross-shelf distribution, with the reticulate morphology generally found closer to the shelf edge than the annulate, and the undulate grading between them but more common to westward (away from the shelf break) (McNeil *et al.*, 2016). This implies that they are probably exposed to differing environmental conditions that control or modulate their growth and morphology. For example, is the undulate morphotype thinner because it grows further away from the shelf edge and possible resource input from shelf-edge upwelling?

The bioherms appear to be constrained to a vertical limit whereby the water depth to bioherm tops is fairly uniform (20–25 m.b.s.l.) for kilometre-scale distances across bioherms. Figure 6D illustrates an example where the antecedent substrate shallows upwards by approximately 10 m due to the gentle gradient of the underlying pre-Holocene continental shelf. But the depth to bioherm tops remains relatively consistent, resulting in a thinning sediment package. On average, the antecedent substrate beneath the undulate morphotype is 4.5 m shallower than the annulate, and the sediment package is on average 6 m thinner. But there is only a 1 m difference in the average bathymetry depth (m.b.s.l.) between undulate and annulate (Table 5). This raises the question of whether bioherm growth is constrained to within *ca* 20–25 m.b.s.l. Skjold (1988) proposed that the upward limit of bioherm growth in Lloyd Bay (GBR, Figure 3) is controlled by wave-base. The bathymetry data would appear to support this, but it is not possible to determine whether this is a true vertical limit, or whether bioherms still have the capacity to fill vertical accommodation space given more time at present sea level. Published *Halimeda* vertical accretion rates from sediment cores in the GBR range from 0.75 to 2.33 m/kyr (Marshall and Davies, 1988; Davies, 2011). These rates imply a potential Holocene thickness of 7.5–23.3 m assuming 10 kyr since initiation (Orme, 1985; Orme and Salama, 1988). Potential vertical accumulation of 23 m is within the range of the present bioherm isochron thickness calculations (Table S5), but also brings the bioherm tops to within the depth of storm

wave energy, thus confounding any conclusive statements about vertical growth limits. Laterally, the eastern extent of the bioherm boundary appears constrained by current flow from inter-reef passages at the continental shelf edge (Figure 5B,F). The western extent may be limited by the availability of nutrients from upwelling (Marshall and Davies, 1988; Wolanski *et al.*, 1988; Drew, 2001; Davies, 2011).

The bioherm thickness (Table 5), area and volume (Table 6) calculations have implications for the size of the bioherm carbonate factory. The size of the carbonate factory and capacity to fill accommodation space varies considerably between the three morphotypes (Table 6). For each morphotype, the relationship between area and volume are not uniform. The annulate morphotype contributes 15% of the planar surface area but 23% of the volume and mass of CaCO_3 (Table 6). The reticulate morphotype fills the same relative volume (23%) but spread over a larger area (20%). The undulate morphotype covers 65% of the bioherm area, but 54% of the CaCO_3 volume. Although the total contribution from undulate is greatest, the comparative contribution as a proportion of area is less because of the significantly lower average thickness. The annulate morphotype has the greatest capacity to fill vertical accommodation space and highest relative carbonate production ($13.58 \text{ Mt CaCO}_3 \text{ km}^{-2}$), while the undulate morphotype has the least ($7.48 \text{ Mt CaCO}_3 \text{ km}^{-2}$). From this, it appears that morphotype is related to growth rate, which in turn may be influenced by cross-shelf gradients in resource availability or limitation. Unfortunately, the paucity of *Halimeda* bioherm sediment cores and published age data prevent further examination of vertical accumulation rate differentiation by morphotype.

A particularly striking difference between morphotypes is the measurably different slopes and terrain complexity (VRM) between annulate and reticulate (Figure 5C,D,H). The reticulate surface topography appears more complex and less structured compared to the regular spatial organization of the annulate morphotype. An important new finding is the consistent difference between the inward and outward-facing slope gradient (8.9° vs 2.9° respectively, Table S2) of the annulate rings, as this may provide new insights into the processes forming these shapes and patterns. For example, the development of stoss and lee slopes in ripple and dune formation provides evidence of fluid flow direction and velocity (Baas, 1978; Allen, 1984), and steep slopes have been related to biological mechanisms in influencing bedform patterns (Noffke, 1999; Van de Vijssel *et al.*, 2020). As the bioherm annulate rings are circular to sub-circular, it is unclear how these shapes and patterns develop. It is necessary to consider whether hydrodynamic flow and relationships to the antecedent substrate influence the formation and spatial patterns of these structures. The BTM Aspect output illustrates that inter-reef passages and channels influence the overall shape of the bioherm boundaries (Figure 5F), presumably because flow velocity has a scouring effect that inhibits *Halimeda*

growth in the channels (Drew and Abel, 1988; Marshall and Davies, 1988; Drew, 2001). However, there is no evidence of any preferred aspect orientation in the shapes and patterns of annulate rings and reticulate mounds (Figure 5F). In marine ecosystems, regular bedform patterns mediated by tidal flow can tend towards elongate parallel to flow direction (e.g., estuarine ridges and runnels Williams *et al.*, 2008; Van de Vijssel *et al.*, 2020), or perpendicular to flow direction (e.g., intertidal seagrass; Van der Heide *et al.*, 2010). In the present study, the bioherm tops are fully subtidal, at *ca* 25 m water depth. In the GBR, flow dynamics at the individual bioherm scale have not been explored, therefore it is not possible to exclude a hydrodynamic (e.g., bottom currents, surface eddies, wave oscillations, etc.) influence on bioherm circular morphology. If hydrodynamics do play a role in shaping the annulate rings, the mechanism(s) would need to be consistent throughout >6,000 km² of bioherm distribution across six degrees of latitude.

4.2 | Internal architecture and antecedent topography

From the 210 km of sub-bottom profiles available to this study, no evidence was found that the antecedent substrate controls the annulate and reticulate shapes and patterns. Hopley, Smithers and Parnell (2007) describe the Pleistocene surface beneath the bioherms as ‘everywhere planar or gently sloping’. Of course, there are some examples where the planar antecedent substrate is incised by palaeochannels or punctuated by submerged reefs (e.g. Figure 7) but bioherms tend not to form on these surfaces, and the observations reported here support this overall planar description beneath the bioherms. The annulate and reticulate crests, and corresponding hollows and valleys that produce up to 25 m of positive relief, do not appear to be inherited from any obvious variation in the antecedent substrate. This is consistent with the interpretation from the much smaller bioherm region in the southern GBR (Searle and Flood, 1988). The submerged coral reefs and pinnacles observed in Figure 7 do appear to initiate off antecedent highs, in contrast with the bioherms, although geomorphological independence from the antecedent substrate has also been demonstrated in some Holocene coral patch reefs (Collins *et al.*, 1996; Blakeway and Hamblin, 2015). The parallel to sub-parallel lamellar bedding and flat surface topography observed in the undulate morphotype does closely follow the planar antecedent topography (Figure 4B). Some authors (Orme *et al.*, 1978; Davies and Marshall, 1985; Drew and Abel, 1985; 1988; Marshall and Davies, 1988) have previously termed these lamellar features as biostromes, *sensu* Cumings (1932). Davies (2011) discusses the association of *Halimeda* meadows, biostromes and bioherms and whether these deposits are representing a

chronological succession. This discussion is useful as it links the disciplines of geology and biology, and introduces the subject of *Halimeda* meadows and their potential biological influence on bioherm development.

4.3 | Biological influence on *Halimeda* bioherm development and stabilization

Hillis (1988) describes the development of lagoonal *Halimeda* meadows at Enewetak Atoll that grow across unconsolidated sediment and produce a vertically ‘raised terrace’ above neighbouring barren sands. The author proposes a model of *Halimeda* meadow growth as an important transition towards *Halimeda* bank (bioherm) development (Hillis, 1988). The growth mechanism at Enewetak is attributed to the extensive *Halimeda* holdfast network and vertical

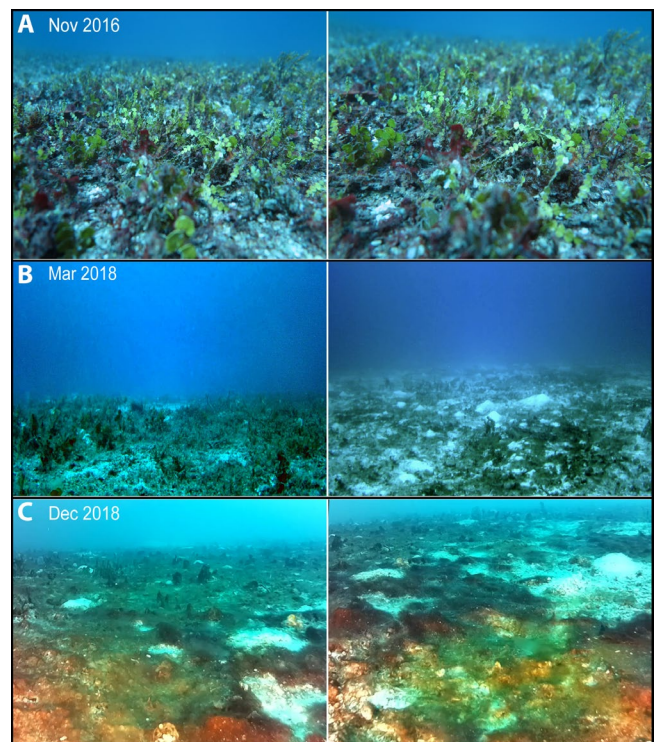


FIGURE 8 A localised die-back of *Halimeda* and subsequent smothering and replacement by algal mats near Lizard Island (see Figure 3). (A) living *Halimeda* meadow at 27 m water depth photographed in November 2016 (credit E. Kennedy); (B) the same site in March 2018 showed evidence of *Halimeda* die-off and partial covering by a filamentous algae (cyanobacteria?); (C) by December 2018 there was no live *Halimeda* and the site was almost completely covered by algal mats with some small bare patches of *Halimeda* sediment. (A) was captured by scuba diver with GoPro camera; (B) and (C) were captured by Remotely Operated Vehicle video that surveyed an area of approximately 250 m². The side-by-side images shown for (A), (B) and (C) extend the horizontal field of view. Field of view in (A) is approximately 1 m; (B) and (C) is approximately 6 m. Unfortunately there was no opportunity to extract samples

build-up of shed segments that are subsequently stabilized by cyanobacterial algal mats. New in-situ *Halimeda* growth accumulates segments which are subsequently stabilized by new algal mats in a repeating cycle (Hillis, 1988). Anecdotal evidence from marine geologists who have scuba-dived on the GBR bioherms in the 1980s do suggest a ‘boom and bust’ growth cycle. Descriptions range from lush and ‘rainforest-like’ (Marshall and Davies, 1988) to a ‘white desert’. Recent photographs from near Lizard Island show abundant lush green growth (Figure 8A), however, there is evidence of a recent localized die-off and phase shift to algal mats at this location (Figure 8C). The photographs of (cyanobacterial?) algal mats (Figure 8C) were captured opportunistically by a remotely operated vehicle while re-visiting a previous dive site. The specific cause of *Halimeda* die-off is unknown, but follows 2 consecutive years of catastrophic marine heat-waves in the GBR (2016 and 2017). The apparent phase shift from *Halimeda* meadow to algal mats may provide some initial evidence of a similar process of cyclical stabilization and aggradation to that described from Enewetak. Recurring phases of cyclical growth/senescence may explain the bedded internal architecture observed in the GBR bioherms, but these are metre-scale thickness seismic features that would be representing centennial to millennial timescales in stratigraphy. A clear mechanism(s) to explain these bedding features remains unresolved, but may involve different biotic and/or abiotic cyclic processes interacting on different timescales (e.g., Williams *et al.*, 2008; Van de Vijssel *et al.*, 2020). A finer-scale seasonal growth/senescence cycle may be overprinted by environmental changes on longer timescales such as climate, cyclones and/or ocean circulation. For example, signals of ‘super-cyclones’ recurring in 100–300 year intervals since at least the mid-Holocene have been recorded in beach ridge sediments along the GBR, (Nott and Hayne, 2001). To resolve the potential mechanisms and timescales requires higher-resolution stratigraphic analysis combining 3D subsurface geophysical analyses with densely spaced, well-correlated sediment cores and geochemical proxies.

4.4 | Potential for biotic self-organization controlling bioherm geomorphology

An emerging area of research in marine carbonate sedimentary systems is autogenic dynamics, or spatial self-organization. Autogenic (self-generating) dynamics and self-organization are increasingly viewed as significant and important sedimentary processes, modulating the formation of biologically constructed features (Budd *et al.*, 2016; Purkis *et al.*, 2016). At the landscape-scale, local interactions between biological and sedimentary processes can induce geomorphological patterns (Weerman *et al.*, 2010), ranging from regular to irregular depending on the feedback mechanism

(Pascual and Guichard, 2005; Rietkerk and Van de Koppel, 2008; Weerman *et al.*, 2012). In Modern reef-related systems, metre to kilometre-scale reticulate patterns have been shown to be biologically mediated, rather than substrate controlled (Blakeway and Hamblin, 2015; Schlager and Purkis, 2015; Purkis *et al.*, 2016). Additionally, Purkis *et al.* (2015) have demonstrated similar morphometric patterns generated by the fossil alga *Palaeoaplysina* and fossil bryozoan *Tubiphytes* in the Barents Sea, suggesting that biological self-organization in sedimentary systems is not unique to Modern reef systems, and may indeed be recorded as far back as Precambrian microbialites (Van de Vijssel *et al.*, 2020).

A key indicator of biotic self-organization is the interaction of scale-dependent feedbacks between living organisms and their environment, acting upon each other (Klausmeier, 1999; Rietkerk and Van de Koppel, 2008; Van de Koppel *et al.*, 2008; Weerman *et al.*, 2012). Short-range positive feedbacks often involve resource concentration, facilitation, or stress amelioration (Klausmeier, 1999; Van de Koppel *et al.*, 2008; Weerman *et al.*, 2010; Liu *et al.*, 2012; Schwarz *et al.*, 2018). Conversely, resource limitation, competition or increased physical stress can induce long-range negative feedbacks (Barbier *et al.*, 2008; Cartenì *et al.*, 2012; Borum *et al.*, 2014; Blakeway and Hamblin, 2015; Vilas *et al.*, 2017a). Feedbacks between geomorphology and plants are increasingly recognized as key drivers shaping a variety of vegetated landscapes (Schwarz *et al.*, 2018). Clonal plants in particular, can exhibit ring-shaped patterns in terrestrial and marine ecosystems (Cartenì *et al.*, 2012; Borum *et al.*, 2014; Ruiz-Reynés *et al.*, 2017; Vilas *et al.*, 2017a). Ring formation in seagrass and algal systems has been shown to result from initial enhanced growth (short-range positive feedback) leading to central dieback from resource limitation (long-range negative feedback) (e.g. oxygen; Vilas *et al.*, 2017a, 2017b) or accumulation of toxins (Borum *et al.*, 2014), resulting in ring-shaped patches.

The spatial patterning in this morphometric and subsurface data, and the potential boom and bust *Halimeda*/algal mat cycling suggests that the GBR bioherm formation and geomorphology may be influenced by biologically modulated self-organization similar to other marine organo-sedimentary systems. The emergence of large-scale structure or patterning can develop from initially homogeneous conditions (Rietkerk and Van de Koppel, 2008; Van de Koppel *et al.*, 2008). This could explain the development of complex bioherm topography initiating from a relatively planar antecedent substrate. However, the significant differences between the geomorphology and growth dynamics of the three morphotypes suggests that the underlying mechanisms and feedbacks are probably non-uniform across the bioherm distribution in space and time. For example, the central dieback seen in other clonal plant systems (Cartenì *et al.*, 2012; Borum *et al.*, 2014; Ruiz-Reynés *et al.*, 2017; Vilas *et al.*, 2017a), may initiate ring formation

in the annulate morphotype. Then ring accretion results from sediment accumulation, enhanced by *Halimeda* trapping, baffling and stabilization. Topographic elevation on the ring crests subsequently enhances access to nutrients (a positive feedback), while nutrient limitation in the hollows (negative feedback) would result in trough deepening. Nutrient limitation may explain the thinner, flatter, undulate morphology. Studies of biofilm-sediment systems (Weerman *et al.*, 2010; 2012; Van de Vijssel *et al.*, 2020) have demonstrated that topographic flattening can result when the scale-dependent feedback (in this case proposed nutrient limitation) is lost or lacking.

Different feedback mechanisms may generate more irregular spatial patterns (Pascual and Guichard, 2005; Rietkerk and Van de Koppel, 2008; Weerman *et al.*, 2012) that are not necessarily self-organized. Irregular patterns (e.g. the bioherm reticulate morphotype) can be triggered by external disruption of the biophysical feedback (Purkis *et al.*, 2016; Van de Vijssel *et al.*, 2020), signalling critical regime shifts in response to environmental change (Scheffer *et al.*, 2001; Pascual and Guichard, 2005; Weerman *et al.*, 2012). The more irregular topography and abrupt truncations seen in the reticulate bedding could be an indication that such critical shifts have occurred. Given their proximity to the shelf edge and association with upwelling via tidal jets (Wolanski *et al.*, 1988; Drew, 2001), one hypothesis is that the reticulate morphotype may be influenced by higher wave/current exposure, as seen in other spatially organized systems (Noffke, 1999; Guichard *et al.*, 2003; Weerman *et al.*, 2012). Additionally, super-cyclones recurring on centennial timescales (Nott and Hayne, 2001) may potentially trigger cyclical regime shifts in the *Halimeda* ecosystem.

These preliminary hypotheses are speculative from the presently available data, and require further research and testing. Future studies should aim to test the *Halimeda* bioherm ecosystem against specific indicators of self-organization which include oscillating consumer-resource interactions, local disturbance-recovery processes (Rietkerk and Van de Koppel, 2008), spatial auto-correlation, and pattern persistence over time (Van de Vijssel *et al.*, 2020). Previous studies on biotic self-organization in marine ecosystems have utilized field-based observations and remote sensing (Temmerman *et al.*, 2007; Weerman *et al.*, 2012; Blakeway and Hamblin, 2015; Purkis *et al.*, 2015; Van de Vijssel *et al.*, 2020), laboratory experiments (Van de Koppel *et al.*, 2008; Borum *et al.*, 2014), and numerical modelling to test mechanisms against field data (Klausmeier, 1999; Van der Heide *et al.*, 2010; Weerman *et al.*, 2010; Carteni *et al.*, 2012; Liu *et al.*, 2012; Ruiz-Reynés *et al.*, 2017; Vilas *et al.*, 2017a). To inform such models and identify probable feedback mechanisms and processes in the *Halimeda* ecosystem requires a better understanding of the local oceanographic regimes at the bioherm scale and of biogeochemical processes such as

nutrient cycling and productivity. Field measurements of *Halimeda* meadow patch size-frequency distributions may inform predictions of external stress or resource limitation (Van der Heide *et al.*, 2010; Weerman *et al.*, 2012), and pattern scaling relationships such as regular, random, clustered, or fractal (Purkis *et al.*, 2015). Additionally, cross-bioherm investigations of species-specific life history traits (Schwarz *et al.*, 2018) would identify whether different *Halimeda* species variation drives variable growth rates and therefore influences geomorphology differentiation between morphotypes.

Nevertheless, whatever mechanisms are responsible for the formation of reticulate patterns and annulate rings, in the GBR these processes have commenced very soon after the marine transgression flooded the continental shelf at the end of the last ice age when Holocene *Halimeda* growth initiated (Orme and Salama, 1988). The proximity of the annulate ring hollows to the antecedent substrate (within 3 m) indicates that vertical aggradation had commenced within centuries (based on estimated vertical accretions rates (Marshall and Davies, 1988) of the marine transgression. Further constraining vertical accretion rates by individual morphotype certainly requires more sedimentological evidence from densely spaced cores and high-resolution radiocarbon dating not presently available.

It is unknown whether the three-dimensional annulate rings are unique to the GBR bioherms, or whether this morphology is common to other Modern *Halimeda* bioherm locations. Continuous reflection seismic profiles from K-Bank (Phipps and Roberts, 1988) and Miskito Channel (Hine *et al.*, 1988) show almost identical (to the GBR) topographical relief and internal bedding in 2D, so it is reasonable to assume that they would also show the same 3D expression if the data were available. To recognize the build-up of bioherms requires high-resolution geophysical multibeam, LiDAR and seismic surveys to identify the characteristic surface and subsurface expression of these features. As global seafloor mapping efforts increase, such as through the Seabed 2030 Project (<https://seabed2030.gebco.net/>) it is probable that more Modern and Late Quaternary *Halimeda* bioherm sites will be discovered. It has been demonstrated that morphometric patterns in Modern carbonate platforms can be applied to the ancient rock record (Purkis *et al.*, 2015). Therefore, self-organization dynamics in Modern bioherm systems could potentially inform palaeo-environmental interpretations of fossil bioherms and phylloid algal mounds on geological timescales.

5 | CONCLUSIONS

Halimeda bioherm geomorphology is much more complex and diverse than previously understood, and clearly

demonstrates morphotype differentiation. By integrating high-resolution geophysical datasets, combining 3D LiDAR bathymetry and quantitative morphometrics with 2D acoustic sub-bottom profiles, the surface geomorphology and internal sedimentary architecture of three *Halimeda* bioherm morphotypes have been characterized through space and time. This is a significant advance on previously available data. The main findings are summarized thus:

1. The annulate, reticulate and undulate morphotypes are distinctly different based on significant heterogeneity in their topography, thickness, internal structure, slope gradients and terrain complexity. By extension, their morphology is probably influenced by differing processes of development and biophysical feedback mechanisms.
2. Morphotype differentiation has implications for the non-uniform development of the *Halimeda* bioherm carbonate factory, rates of sediment aggradation and progradation, and capacity to fill accommodation space.
3. The lateral boundaries between the three morphotypes merge into one another with no apparent geological influence or change in the antecedent substrate, which is typically planar or gently sloping throughout. This is in contrast with adjacent submerged coral reefs that appear to initiate on topographic highs. Morphotype transitions may be reflecting cross-shelf gradients in biophysical growth limiting processes (e.g. access to nutrients and oxygenation), rather than geological mechanisms.
4. The apparent internal bedding seen in sub-bottom profile in all three morphotypes may result from a combination of biotic or abiotic factors operating at different timescales (e.g., cyclical *Halimeda* growth and death, stabilized by phases of algal mat development, or response to physical disturbance such as cyclones. To resolve the precise mechanisms and timescales involved requires further analysis, in particular stratigraphic correlations with densely spaced sediment cores.
5. One hypothesis is that biological spatial self-organization similar to reticulate reef patterns and other marine organo-sedimentary systems modulates, or at least contributes to, Modern *Halimeda* bioherm geomorphology, in particular the annulate morphotype.

These findings resolve some knowledge gaps, and raise new questions for future work, particularly in developing new testable hypotheses around the mechanisms of potential spatial self-organization. This work contributes a new morphological and morphometric framework to develop field, laboratory and numerical modelling experiments to address these knowledge gaps. Additionally, these results provide geomorphological context to the role of *Halimeda* bioherms in the provision of complex benthic habitat terrain in the inter-reef seascape of the GBR. These results reinforce the importance of the *Halimeda* bioherms to

the GBR's World Heritage Area status and Outstanding Universal Value from a geological and geomorphological perspective.

ACKNOWLEDGMENTS

Our thanks to Elias Samankassou and Dierk Hebbeln for convening the session titled 'Carbonate mounds through time and space' at the 20th International Sedimentological Congress in Quebec City 2018, out of which this publication arose. We acknowledge and thank Geoscience Australia and the Australian Hydrographic Office for the source bathymetry data used in this study, in particular access to the LADS LiDAR data. This research was supported by a grant of sea time on RV *Southern Surveyor* from the CSIRO Marine National Facility. Thanks to Emma Kennedy for permission to use photographs in Figures 1 and 8. The GIS analysis was supported by a science grant from The Ian Potter Foundation awarded to LN and MM. Fieldwork in the Great Barrier Reef Marine Park was undertaken under research permit G17-39618.1 and funded by support from the National Geographic Society (EC-190R-18), The National Parks and Wildlife Foundation, and the Great Barrier Reef Marine Park Authority 'Reef Guardians' science grants awarded to MM. The authors declare no conflicts of interest.

DATA AVAILABILITY STATEMENT

The external datasets that support the findings of this study are detailed in Table S1. The bathymetry DEM and metadata may be accessed from <http://pid.geoscience.gov.au/dataset/ga/115066>. The Topas sub-bottom profile metadata may be accessed from https://www.cmar.csiro.au/data/trawler/survey_details.cfm?survey=S00809.

ORCID

Mardi A. McNeil  <https://orcid.org/0000-0003-4613-4445>
 Luke D. Nothdurft  <https://orcid.org/0000-0001-9646-9070>
 Nicholas J. Dyriw  <https://orcid.org/0000-0002-1783-084X>
 Jody M. Webster  <https://orcid.org/0000-0002-0005-6448>
 Robin J. Beaman  <https://orcid.org/0000-0003-3972-9862>

REFERENCES

- Abbey, E., Webster, J.M. and Beaman, R.J. (2011) Geomorphology of submerged reefs on the shelf edge of the Great Barrier Reef: the influence of oscillating Pleistocene sea-levels. *Marine Geology*, 288, 61–78.
- Abbey, E., Webster, J.M., Braga, J.C., Jacobsen, G.E., Thorogood, G., Thomas, A.L. *et al.* (2013) Deglacial mesophotic reef demise on the Great Barrier Reef. *Palaeogeography, Palaeoclimatology, Palaeoecology*, 392, 473–494.
- Allen, J. (1984) *Sedimentary Structures, Their Character and Physical Basis*. Developments in Sedimentology 30. Amsterdam: Elsevier.
- Baas, J.H. (1978). *Ripple, Ripple Mark, Ripple Structure*. Sedimentology. Berlin, Heidelberg: Springer, Berlin Heidelberg.

- Barbier, N., Couteron, P., Lefever, R., Deblauwe, V. and Lejeune, O. (2008) Spatial decoupling of facilitation and competition at the origin of gapped vegetation patterns. *Ecology*, 89, 1521–1531.
- Beaman, R. (2010). 3DGBR: A high-resolution depth model for the Great Barrier Reef and Coral Sea. Marine and Tropical Sciences Facility (MTSRF) Project, 2. Available at: <https://www.deeppref.org/publications/reports/67-3dgb-final.html>
- Beaman, R.J. (2017). High-resolution depth model for the Great Barrier Reef – 30 m. Available at: <http://pid.geoscience.gov.au/datas/et/115066>
- Blakeway, D. and Hamblin, M.G. (2015) Self-generated morphology in lagoon reefs. *PeerJ*, 3, e935.
- Blanchon, P. (2011) Geomorphic zonation. In: Hopley, D. (Ed.) *Encyclopedia of Modern Coral Reefs: Structure, Form and Process*. Dordrecht: Springer Netherlands.
- Bonney, T.G. (1898) The boring at Funafuti. *Nature*, 59, 29.
- Borum, J., Raun, A.L., Hasler-Sheetal, H., Pedersen, M.Ø., Pedersen, O. and Holmer, M. (2014) Eelgrass fairy rings: sulfide as inhibiting agent. *Marine Biology*, 161, 351–358.
- Bosellini, F.R., Russo, A. and Vescogni, A. (2002) The Messinian reef complex of the Salento Peninsula (southern Italy): Stratigraphy, facies and paleoenvironmental interpretation. *Facies*, 47, 91–112.
- Braga, J.C., Martín, J.M. and Riding, R. (1996) Internal structure of segment reefs: *Halimeda* algal mounds in the Mediterranean Miocene. *Geology*, 24, 35–38.
- Budd, D.A., Hajek, E.A. and Purkis, S.J. (2016) Introduction to autogenic dynamics and self-organization in sedimentary systems. *SEPM (Society for Sedimentary Geology) Special Publication*, 106, 1–4.
- Carteni, F., Marasco, A., Bonanomi, G., Mazzoleni, S., Rietkerk, M. and Giannino, F. (2012) Negative plant soil feedback explaining ring formation in clonal plants. *Journal of Theoretical Biology*, 313, 153–161.
- Chapman, F. and Mawson, D. (1906) On the importance of *Halimeda* as a reef-forming organism: with a description of the *Halimeda* limestones of the New Hebrides. *Quarterly Journal of the Geological Society*, 62, 702.
- Clifton, K.E. (1997) Mass spawning by green algae on coral reefs. *Science*, 275, 1116–1118.
- Collins, L.B., Zhu, Z.R. and Wyrwoll, K.H. (1996) The structure of the Easter Platform, Houtman Abrolhos reefs: Pleistocene foundations and Holocene reef growth. *Marine Geology*, 135, 1–13.
- Cummings, E.R. (1932) Reefs or bioherms? *Geological Society of America Bulletin*, 43, 331–352.
- Davies, P. (2011) *Halimeda* bioherms. In: Hopley, D. (Ed.) *Encyclopaedia of Modern Coral Reefs; Structure, form and process*. Dordrecht: Springer.
- Davies, P. and Marshall, J. (1985) *Halimeda* bioherms – low energy reefs, northern Great Barrier Reef. Proceedings of the 5th International Coral Reef Symposium, 1–7.
- Dragastan, O.N. and Herbig, H.-G. (2007) *Halimeda* (green siphonous algae) from the Paleogene of (Morocco) – taxonomy, phylogeny and paleoenvironment. *Micropaleontology*, 53, 1–72.
- Drew, E. (1983) *Halimeda* biomass, growth rates and sediment generation on reefs in the central Great Barrier Reef province. *Coral Reefs*, 2, 101–110.
- Drew, E. (2001) Ocean nutrients to sediment banks via tidal jets and *Halimeda* meadows. In: Wolanski, E. (Ed.) *Oceanographic Processes of Coral Reefs: Physical and Biological Links in the Great Barrier Reef* (pp. 255–267). Boca Raton, FL: CRC Press.
- Drew, E. and Abel, K. (1985). Biology, sedimentology and geography of the vast inter-reefal *Halimeda* meadows within the Great Barrier Reef Province. Proceedings of the 5th International Coral Reef Symposium, 15–20.
- Drew, E. and Abel, K. (1988) Studies on *Halimeda*. *Coral Reefs*, 6, 207–218.
- Elliott, G.F. (1965) The interrelationships of some Cretaceous Codiaceae (calcareous algae). *Palaeontology*, 8, 199–203.
- Freile, D., Milliman, J.D. and Hillis, L. (1995) Leeward bank margin *Halimeda* meadows and draperies and their sedimentary importance on the western Great Bahama Bank slope. *Coral Reefs*, 14, 27–33.
- Ginsburg, R., Harris, P., Eberli, G.P. and Swart, P.K. (1991) The growth potential of a bypass margin, Great Bahama Bank. *Journal of Sedimentary Research*, 61, 976–987.
- Guichard, F., Halpin, P., Allison, G., Lubchenko, J. and Menge, B. (2003) Mussel disturbance dynamics: Signatures of oceanographic forcing from local interactions. *The American Naturalist*, 161, 889–904.
- Guppy, H.B. (1887) *The Solomon Islands: Their Geology, General Features, and Suitability for Colonization*. S. Sonnenschein, Lowrey & Company.
- Heyward, A., Pinceratto, E. and Smith, L. (1997) Big Bank Shoals of the Timor Sea: an environmental resource atlas. Australian Institute of Marine Science & BHP Petroleum.
- Hillis, L. (1988). Characteristics of *Halimeda* meadows, with emphasis on a meadow near Enewetak Islet, Enewetak Atoll (Marshall Islands). Proceedings of the sixth International Coral Reef Symposium, 119–125.
- Hillis, L. (1997). Coralgal reefs from a calcareous green alga perspective, and a first carbonate budget. Proceedings of the 8th International Coral Reef Symposium, 761–766.
- Hillis, L.W. (2001) The calcareous reef alga *Halimeda* (Chlorophyta, Byrropsidales): a cretaceous genus that diversified in the cenozoic. *Palaeogeography, Palaeoclimatology, Palaeoecology*, 166, 89–100.
- Hillis-Colinvaux, L. (1980) Ecology and taxonomy of *Halimeda*: primary producer of coral reefs. In: Blaxter, J.H.S., Russell, F.S. and Yonge, M. (Eds.) *Advances in Marine Biology*. Cambridge, MA: Academic Press.
- Hinde, G.J. (1904) *Report on the materials from the borings at the Funafuti Atoll. The Atoll at Funafuti: Borings Into a Coral Reef and the Results*. London: Royal Society Coral Reef Committee Report.
- Hine, A.C., Hallock, P., Harris, M.W., Mullins, H.T., Belknap, D.F. and Jaap, W.C. (1988) *Halimeda* bioherms along an open seaway: Miskito Channel, Nicaraguan Rise, SW Caribbean Sea. *Coral Reefs*, 6, 173–178.
- Hinestrosa, G., Webster, J.M., Beaman, R.J. and Anderson, L.M. (2014) Seismic stratigraphy and development of the shelf-edge reefs of the Great Barrier Reef, Australia. *Marine Geology*, 353, 1–20.
- Hopley, D., Smithers, S.G. and Parnell, K.E. (2007) *The Geomorphology of the Great Barrier Reef: Development, Diversity, and Change*. Cambridge: Cambridge University Press.
- Kirkland, B., Moore, C. Jr and Dickson, J. (1993) Well preserved, aragonitic phylloid algae (Eugonophyllum, Udoteaceae) from the Pennsylvanian Holder Formation, Sacramento Mountains, New Mexico. *Palaos*, 8, 111–120.
- Klausmeier, C.A. (1999) Regular and irregular patterns in semiarid vegetation. *Science*, 284, 1826.

- Lecours, V., Dolan, M.F., Micallef, A. and Lucieer, V.L. (2016) A review of marine geomorphometry, the quantitative study of the seafloor. *Hydrology and Earth System Sciences*, 20, 3207.
- Liu, Q.-X., Weerman, E.J., Herman, P.M., Olff, H. and Van de Koppel, J. (2012) Alternative mechanisms alter the emergent properties of self-organization in mussel beds. *Proceedings of the Royal Society B: Biological Sciences*, 279, 2744–2753.
- Lundblad, E.R., Wright, D.J., Miller, J., Larkin, E.M., Rinehart, R., Naar, D.F. et al. (2006) A benthic terrain classification scheme for American Samoa. *Marine Geodesy*, 29, 89–111.
- Marshall, J.F. and Davies, P.J. (1988) *Halimeda* bioherms of the northern Great Barrier Reef. *Coral Reefs*, 6, 139–148.
- Martin, J.M., Braga, J.C. and Riding, R. (1997) Late Miocene *Halimeda* alga-microbial segment reefs in the marginal Mediterranean Sorbas Basin, Spain. *Sedimentology*, 44, 441–456.
- Mathews, E., Heap, A. and Woods, M. (2007) *Inter-Reefal Seabed Sediments and Geomorphology of the Great Barrier Reef: A Spatial Analysis*. Canberra, ACT: Geoscience Australia, Record 2007/09.
- Maxwell, W. (1973) Sediments of the great barrier reef province. In: Jones, O. and Endean, R. (Eds.) *Biology and Geology of Coral Reefs*. New York: Academic.
- McNeil, M.A., Webster, J.M., Beaman, R.J. and Graham, T.L. (2016) New constraints on the spatial distribution and morphology of the *Halimeda* bioherms of the Great Barrier Reef, Australia. *Coral Reefs*, 35, 1343–1355.
- Milliman, J.D. (1993) Production and accumulation of calcium carbonate in the ocean: Budget of a nonsteady state. *Global Biogeochemical Cycles*, 7, 927–957.
- Noffke, N. (1999) Erosional remnants and pockets evolving from biotic–physical interactions in a recent lower supratidal environment. *Sedimentary Geology*, 123, 175–181.
- Nott, J. and Hayne, M. (2001) High frequency of ‘super-cyclones’ along the Great Barrier Reef over the past 5,000 years. *Nature*, 413, 508–512.
- Orme, G. (1985). The sedimentological importance of *Halimeda* in the development of back reef lithofacies, northern Great Barrier Reef (Australia). Proceedings of the 5th International Coral Reef Symposium, 31–37.
- Orme, G.R. and Salama, M.S. (1988) Form and seismic stratigraphy of *Halimeda* banks in part of the northern Great Barrier Reef Province. *Coral Reefs*, 6, 131–137.
- Orme, G., Flood, P.G. and Sargent, G. (1978) Sedimentation trends in the lee of outer (ribbon) reefs, northern region of the Great Barrier Reef province. *Philosophical Transactions of the Royal Society of London A: Mathematical, Physical and Engineering Sciences*, 291, 85–99.
- Pascual, M. and Guichard, F. (2005) Criticality and disturbance in spatial ecological systems. *Trends in Ecology & Evolution*, 20, 88–95.
- Passalacqua, P., Belmont, P., Staley, D.M., Simley, J.D., Arrowsmith, J.R., Bode, C.A. et al. (2015) Analyzing high resolution topography for advancing the understanding of mass and energy transfer through landscapes: a review. *Earth-Science Reviews*, 148, 174–193.
- Phipps, C.V.G. and Roberts, H.H. (1988) Seismic characteristics and accretion history of *Halimeda* bioherms on Kalukalukuang Bank, eastern Java Sea (Indonesia). *Coral Reefs*, 6, 149–159.
- Purkis, S.J., Rowlands, G., Riegl, B. and Renaud, P. (2010) The paradox of tropical karst morphology in the coral reefs of the arid Middle East. *Geology*, 38, 227–230.
- Purkis, S., Casini, G., Hunt, D. and Colpaert, A. (2015) Morphometric patterns in modern carbonate platforms can be applied to the ancient rock record: similarities between Modern Alacranes Reef and Upper Palaeozoic platforms of the Barents Sea. *Sedimentary Geology*, 321, 49–69.
- Purkis, S., Van De Koppel, J. and Burgess, P. (2016) Spatial self-organization in carbonate depositional environments. *SEPM (Society for Sedimentary Geology) Special Publication*, 106, 53–66.
- Rao, V.P., Veerayya, M., Nair, R.R., Dupeuble, P.A. and Lamboy, M. (1994) Late Quaternary *Halimeda* bioherms and aragonitic faecal pellet-dominated sediments on the carbonate platform of the western continental shelf of India. *Marine Geology*, 121, 293–315.
- Rao, V.P., Mahale, V. and Chakraborty, B. (2018) Bathymetry and sediments on the carbonate platform off western India: Significance of *Halimeda* bioherms in carbonate sedimentation. *Journal of Earth System Science*, 127, 106.
- Rees, S.A., Opdyke, B.N., Wilson, P.A. and Henstock, T.J. (2007) Significance of *Halimeda* bioherms to the global carbonate budget based on a geological sediment budget for the Northern Great Barrier Reef, Australia. *Coral Reefs*, 26, 177–188.
- Rietkerk, M. and Van De Koppel, J. (2008) Regular pattern formation in real ecosystems. *Trends in Ecology & Evolution*, 23, 169–175.
- Roberts, H.H., Phipps, C.V. and Effendi, L. (1987) *Halimeda* bioherms of the eastern Java Sea, Indonesia. *Geology*, 15, 371–374.
- Roberts, H.H., Aharon, P. and Phipps, C.V. (1988) Morphology and sedimentology of *Halimeda* bioherms from the eastern Java Sea (Indonesia). *Coral Reefs*, 6, 161–172.
- Ruiz-Reynés, D., Gomila, D., Sintes, T., Hernández-García, E., Marbà, N. and Duarte, C.M. (2017) Fairy circle landscapes under the sea. *Science Advances*, 3, e1603262.
- Sappington, J.M., Longshore, K.M. and Thompson, D.B. (2007) Quantifying landscape ruggedness for animal habitat analysis: a case study using bighorn sheep in the Mojave Desert. *The Journal of wildlife management*, 71, 1419–1426.
- Scheffer, M., Carpenter, S., Foley, J.A., Folke, C. and Walker, B. (2001) Catastrophic shifts in ecosystems. *Nature*, 413, 591–596.
- Schlager, W. and Purkis, S. (2015) Reticulate reef patterns – antecedent karst versus self-organization. *Sedimentology*, 62, 501–515.
- Schwarz, C., Gourgue, O., Van Belzen, J., Zhu, Z., Bouma, T.J., Van De Koppel, J. et al. (2018) Self-organization of a biogeomorphic landscape controlled by plant life-history traits. *Nature Geoscience*, 11, 672–677.
- Searle, D. and Flood, P. (1988). *Halimeda* bioherms of the Swain reefs – southern Great Barrier Reef. Proceedings of the 6th International Coral Reef Symposium, 139–144.
- Skjold, L.J. (1988). A seismic and sedimentary study of the late Quaternary development of the Lloyd Bay area, northern Great Barrier Reef, Australia. PhD Thesis. University of Queensland, <https://espace.library.uq.edu.au/view/UQ:364822>
- Temmerman, S., Bouma, T., Van De Koppel, J., van der Wal, D., De Vries, M. and Herman, P. (2007) Vegetation causes channel erosion in a tidal landscape. *Geology*, 35, 631–634.
- Tilbrook, B. and Matear, R.J. (2008). Voyage summary SS09/2008, CSIRO Marine National Facility, Hobart, Australia, pp.17. Retrieved from: https://www.cmar.csiro.au/data/reporting/get_file.cfm?eov_pub_id=994
- Van de Koppel, J., Gascoigne, J.C., Theraulaz, G., Rietkerk, M., Mooij, W.M. and Herman, P.M. (2008) Experimental evidence for spatial self-organization and its emergent effects in mussel bed ecosystems. *Science*, 322, 739–742.
- Van der Heide, T., Bouma, T.J., van Nes, E.H., Van De Koppel, J., Scheffer, M., Roelofs, J.G.M. et al. (2010) Spatial self-organized

- patterning in seagrasses along a depth gradient of an intertidal ecosystem. *Ecology*, *91*, 362–369.
- Van de Vijssel, R.C., van Belzen, J., Bouma, T.J., van der Wal, D., Cussedu, V., Purkis, S.J. *et al.* (2020) Estuarine biofilm patterns: Modern analogues for Precambrian self-organization. *Earth Surface Processes and Landforms*, *45*, 1141–1154.
- Vilas, M.P., Adams, M.P., Oldham, C.E., Marti, C.L. and Hipsey, M.R. (2017a) Fragment dispersal and plant-induced dieback explain irregular ring-shaped pattern formation in a clonal submerged macrophyte. *Ecological Modelling*, *363*, 111–121.
- Vilas, M.P., Marti, C.L., Adams, M.P., Oldham, C.E. and Hipsey, M.R. (2017b) Invasive macrophytes control the spatial and temporal patterns of temperature and dissolved oxygen in a shallow lake: a proposed feedback mechanism of macrophyte loss. *Frontiers in Plant Science*, *8*, 2097.
- Walbridge, S., Slocum, N., Pobuda, M. and Wright, D. (2018) Unified geomorphological analysis workflows with Benthic Terrain Modeler. *Geosciences*, *8*, 94.
- Weerman, E.J., Van De Koppel, J., Eppinga, M.B., Montserrat, F., Liu, Q.-X. and Herman, P.M. (2010) Spatial self-organization on intertidal mudflats through biophysical stress divergence. *The American Naturalist*, *176*, E15–E32.
- Weerman, E., van Belzen, J., Rietkerk, M., Temmerman, S., Kéfi, S., Herman, P. *et al.* (2012) Changes in diatom patch-size distribution and degradation in a spatially self-organized intertidal mudflat ecosystem. *Ecology*, *93*, 608–618.
- Whiteway, T., Smithers, S., Potter, A. and Brooke, B. (2013) Geological and geomorphological features of outstanding universal value in the Great Barrier Reef World Heritage Area. Report prepared for SEWPaC. Coastal Marine and Climate Change Group, Geoscience Australia and School of Earth and Environmental Sciences. James Cook University, Townsville, Australia.
- Williams, J.J., Carling, P.A., Amos, C.L. and Thompson, C. (2008) Field investigation of ridge–runnel dynamics on an intertidal mudflat. *Estuarine, Coastal and Shelf Science*, *79*, 213–229.
- Wolanski, E., Drew, E., Abel, K.M. and O'Brien, J. (1988) Tidal jets, nutrient upwelling and their influence on the productivity of the alga *Halimeda* in the Ribbon Reefs, Great Barrier Reef. *Estuarine, Coastal and Shelf Science*, *26*, 169–201.
- Wray, J.L. (1977) *Calcareous Algae*. Amsterdam: Elsevier.

SUPPORTING INFORMATION

Additional supporting information may be found online in the Supporting Information section.

How to cite this article: McNeil MA, Nothdurft LD, Dyriw NJ, Webster JM, Beaman RJ. Morphotype differentiation in the Great Barrier Reef *Halimeda* bioherm carbonate factory: Internal architecture and surface geomorphometrics. *Depositional Rec.* 2020;00:1–24. <https://doi.org/10.1002/dep2.122>